Title

An Investigation into the Effects of Mn Promotion on the Activity and Selectivity of Co/SiO2 for Fischer–Tropsch Synthesis: Evidence for Enhanced CO Adsorption and Dissociation

Journal

ACS Catalysis, 5(10)

ISSN

2155-5435

Authors

Johnson, Gregory R
Werner, Sebastian
Bell, Alexis T

Publication Date

2015-10-02

DOI

10.1021/acscatal.5b01578

Peer reviewed

An Investigation into the Effects of Mn-Promotion on the Activity and Selectivity of Co/SiO_2 for Fischer-Tropsch Synthesis: Evidence for Enhanced CO Adsorption and Dissociation

Gregory R. Johnson[a], Sebastian Werner[a], Alexis T. Bell[a,b,*]

[a] Department of Chemical and Biomolecular Engineering, University of California, Berkeley, CA 94720, USA

[b] Chemical Sciences Division, Lawrence Berkeley National Laboratory, Berkeley, CA 94720, USA

Submitted to

ACS Catalysis

July 23, 2015

*corresponding author: bell@cchem.berkeley.edu

Abstract

Mn is an effective promoter for improving the activity and selectivity of Co-based Fischer-Tropsch synthesis (FTS) catalysts, but the mechanism by which this promoter functions is poorly understood. The work reported here was aimed at defining the manner in which Mn interacts with Co and how these interactions affect the activity and selectivity of Co. Detailed measurements are reported for the kinetics of FTS as a function of Mn/Co ratio, temperature, and reactant partial pressures. These data are described by a single, two-parameter rate expression. Mn-promotion was found to increase both the apparent rate constant for CO consumption and the CO adsorption constant. Further evidence for enhanced CO adsorption and dissociation was obtained from measurements of temperature-programmed desorption of CO and CO disproportionation rates, respectively. Quantitative analysis of elemental maps obtained by STEM-EDS revealed that the promoter accumulates preferentially on the surface of Co nanoparticles at low Mn loadings, resulting in a rapid onset of improvements in the product selectivity as the Mn loading increases. For catalysts prepared with loadings higher than Mn/Co = 0.1, the additional Mn accumulates in the form of nanometer-scale particles of MnO on the support. In situ IR spectra of adsorbed CO show that Mn promotion increases the abundance of adsorbed CO with weakened C–O bonds. It is proposed that the cleavage of the C–O bond is promoted through Lewis acid-base interactions between the Mn^{2+} cations located at the edges of MnO islands covering the Co nanoparticles and the O atom of CO adsorbates adjacent to the MnO islands. The observed decrease in selectivity to CH_4 and the increased selectivity to C_{5+} products with increasing Mn/Co ratio are attributed to a decrease in the ratio of adsorbed H to CO on the surface of the supported Co nanoparticles.

Keywords

Fischer-Tropsch Synthesis, Heterogeneous Catalysis, Cobalt, Manganese, Promotion

1. Introduction

Fischer-Tropsch synthesis (FTS) is used as a process for converting natural gas and coal-derived synthesis gas to long-chain hydrocarbons. Recent expansions of worldwide FTS production capacity and the growing number of academic studies on the topic demonstrate the ongoing interest in this chemical process (*1*). The contemporary abundance of natural gas and high market demand for diesel fuel in many parts of the world has focused attention toward Co-based FTS catalysts, which are widely considered to be the optimal catalyst choice for this application (*2*). One of the chief requirements for Co-based FTS processes to be economically viable is a high selectivity toward C_{5+} hydrocarbons together with a low selectivity to byproducts such as methane. Product selectivity can be improved by adjusting process conditions (e.g., lower temperature, higher pressure, and lower syngas H_2:CO ratios), as well as by optimizing catalyst composition and structure. The use of non-catalytically active elements to promote catalyst activity, selectivity, or stability is a well-investigated topic in the context of Co-based FTS catalysts. Most studies have focused on the inclusion of noble metals to assist the reduction of Co to the active metallic state (*3*). These elements are typically reported to have limited or occasionally detrimental effects on the FTS product distribution (*4*), but a variety of elements have been demonstrated to consistently decrease the selectivity toward methane and shift the products toward higher molecular weights (*5*) (*6*) (*7*). Of the elements having positive effects on the product distribution, Mn is among the most frequently discussed in the open literature.

Early studies concerning the use of MnO as a support material demonstrated that this support decreased the selectivity to methane and increased the olefin to paraffin ratio of light hydrocarbons compared to more conventional supports (*8*) (*9*) (*10*). Within the past decade, research by Morales et al. (*11*) (*12*) (*13*) and de Jong et al. (*14*) (*15*) have explored the use of Mn as a promoter for Co FTS catalysts. In addition to observing selectivity and rate enhancements in the promoted catalysts, these researchers found evidence that Mn forms a variety of oxide structures, parts of which were associated with the active Co phase. Feltes et al. studied the effect of catalyst preparation methods using impregnation solvent pH to guide the selective deposition of the Mn promoter onto the Co (*16*) (*17*). This strategy was reported to yield promotion effects comparable to those obtained by dry impregnation but requiring smaller quantities of the Mn promoter owing to the improved contact between the Mn and the Co. Relatedly, we have carried out quantitative analyses of elemental maps of catalysts prepared by different pretreatment conditions and demonstrated that Mn promotion effects are correlated with the degree of spatial colocation between Mn and Co (*18*). Dinse et al. have examined the activity and selectivity of silica-supported Co-

Mn catalysts and rationalized the promotion effects in terms of H availability and CO coverage (*19*). More recently, several studies have reported measurements of the CO hydrogenation kinetics over Mn-promoted Co FTS catalysts, but these investigations have not provided much additional insight into how Mn participates in the FTS chemistry (*20*) (*21*) (*22*).

While the effects of Mn promotion on FTS over Co are now well-documented, the manner by which Mn promotion affects catalyst activity and selectivity remains speculative and untested. The most frequently cited explanation for the effects of metal oxide promoters on CO hydrogenation over Rh assumes that CO adsorbed at the metal-metal oxide interface can interact with both the metal through the C atom and with a cation of the oxide through the O atom (*23*) (*24*). The promoter is hypothesized to serve as a Lewis acid that weakens the C–O bond and facilitates its dissociation. By analogy to Rh catalysts, a direct interaction between the CO and promoter cation at interface sites has been invoked as an explanation for the promotion effects seen in Co-based catalysts (*25*). Nevertheless, there have been no attempts to determine whether the CO adsorption at the metal-promoter interface results in stronger CO adsorption and enhanced dissociation of the C–O bond other than by inferences drawn from observations of the effects of oxide promoters on FTS kinetics. We report here an investigation of Mn-promoted Co-based FTS catalysts that combines detailed catalyst characterization data with measurements of the reaction kinetics. These efforts were undertaken with the aim of clarifying the chemical basis for the observed effects of Mn-promotion of Co. In addition to determining how Mn affects the FTS rate law, connections were established between catalyst structure and performance that explain the dependence of FTS activity and selectivity on promoter loading. These findings strongly favor the hypothesis that active sites near the Co-MnO interface are responsible for the improved activity and C_{5+} selectivity of Mn-promoted Co catalysts.

2. Experimental

2.1 Catalyst Synthesis

The catalysts were prepared by incipient wetness impregnation of silica powder (PQ-Corporation, CS-2129). Typically, 2.5 ml of an aqueous solution of $Co(NO_3)_2{\cdot}6H_2O$ and $Mn(CH_3COO)_2{\cdot}4H_2O$ (Sigma-Aldrich, 99.999 % purity) was added drop-wise to 1 g of the support material, which was constantly stirred. The quantities of dissolved Co and Mn precursors in the solution were adjusted so as to keep the loading of Co fixed at 10 wt% with respect to the sum of silica and cobalt and to achieve various molar ratios of Mn to Co between 0 and 0.5. After drying the catalyst precursor overnight at room temperature, the dried

material was passed through a 60 mesh sieve and the retained particles were discarded. The silica containing the metal precursor was then heated to 673 K in H_2 as described in the Supporting Information in order to decompose the precursors and reduce the Co. The catalyst was then cooled to room temperature and passivated. Catalyst compositions were verified by ICP-EOS (Galbraith Laboratories).

2.2 TEM Imaging

The passivated catalysts were prepared for analysis by electron microscopy by drop-casting ethanol suspensions of ground catalyst onto lacey carbon Cu TEM grids (Ted Pella). A complete description of this protocol is given in the Supporting Information. To determine size distributions of the catalyst nanoparticles, bright-field transmission electron microscopy (BF-TEM) images of the Co-Mn catalysts were acquired at the Electron Microscopy Lab at the University of California, Berkeley using an FEI Tecnai T12 electron microscope. Imaging was done with an accelerating voltage of 120 kV. Nanoparticle size distributions for each sample were determined using samples of approximately 300 nanoparticles. The surface mean diameters for the nanoparticles in a catalyst sample were calculated according to Eq. (1), where n_i is the number of particles with diameter d_i in a nanoparticle sample of size N (*26*):

$$\bar{d} = \frac{\sum_i^N n_i d_i^3}{\sum_i^N n_i d_i^2} \quad (1)$$

2.3 STEM-EDS Elemental Mapping

Elemental maps of the catalysts were acquired using scanning transmission electron microscopy with energy dispersive spectroscopy (STEM-EDS). The samples for this analysis were prepared using the same protocol as was used for preparing the BF-TEM samples. STEM-EDS measurements were done using an FEI Titan electron microscope at the National Center for Electron Microscopy at the Lawrence Berkeley National Laboratory. The microscope was operated with an accelerating voltage of 200 kV and fluorescent X-rays were collected using a Bruker, four-segment, silicon drift detector. A complete description of the spectrometer settings and analysis methods are given in the Supporting Information.

2.4 Chemisorption and Titration Characterizations

Static H_2 chemisorption measurements were acquired using a Micromeritics 3Flex surface characterization analyzer. Passivated catalyst samples were placed inside a quartz sample tube and heated to 673 K in H_2 to reduce the Co. After flowing H_2 at this temperature for 2 h, the sample tubes were evacuated and cooled to 373 K, which was the temperature at which the adsorption isotherms

were measured. This choice of adsorption temperature was based on the published finding that 373 K leads to maximum H_2 uptake for Co supported on silica (*27*). The total H_2 uptake from the isotherm was used to calculate the number of metallic Co atoms exposed on the surface of the nanoparticles for a given catalyst sample. Based on published results for similar catalysts, it was assumed that the H:Co adsorption stoichiometry was 1:1 (*27*) (*28*).

O_2 titration was used to assess the extent of Co reduction in the reduced catalyst samples. These measurements were done by monitoring the effluent of a quartz glass reactor with an MKS Spectra Minilab quadrupole mass spectrometer. Catalyst samples were loaded into the reactor and reduced at 673 K in H_2. Using a sample loop, pulses of air were injected into the reactor using He as a carrier gas. The O_2 peaks in the mass spectrometry data were integrated to obtain O_2 uptake values due to oxidation of the Co and Mn. Based on data from X-ray adsorption spectroscopy, it was assumed that the Co initially consisted of a mixture of Co(0) and CoO that was oxidized completely to Co_3O_4 and that all the Mn underwent an oxidation from MnO to MnO_2. Accordingly, the extent of reduction of the Co was calculated as shown in Eq. (2):

$$frac.\,Co\ reduced = \frac{2(O_2\ molar\ uptake) - (moles\ Mn) - \left(\frac{4}{3} - 1\right)(moles\ Co)}{moles\ Co} \qquad (2)$$

CO temperature programmed desorption experiments were conducted using a Micromeritics AutoChem II 2920. Passivated catalyst samples were reduced at 4 K/min to 673 K in H_2 with a 2 h hold at 673 K and then cooled to 213 K with He flowing through the system. After the temperature had stabilized, CO pulses were introduced to the sample using He as the carrier gas while monitoring the flow downstream of the sample using the instrument thermal conductivity detector. The CO pulses continued until the sample showed no further CO uptake, and the sample tube was flushed for 10 min to clear any CO in the gas phase. The temperature was then ramped to 1073 K at 10 K/min to desorb chemisorbed CO from the catalyst surface.

2.5 X-Ray Diffraction

Powder X-ray diffraction (XRD) patterns were collected at beamline 11-BM at the Advanced Photon Source synchrotron at Argonne National Laboratory using the mail-in service. Passivated catalyst samples were reduced at 673 K in H_2 and then rapidly cooled to 298 K in flowing He. Under inert atmosphere, the reduced samples were then transferred into Kapton sample tubes and sealed with epoxy. XRD

measurements were conducted at ambient temperature using 28.3 keV X-rays over a 2θ range of 0.5 ° to 50 ° with a 0.001 ° step size.

2.6 In Situ X-Ray Absorption Spectroscopy

X-ray absorption spectroscopy (XAS) data were collected in transmission mode at beamline 10-BM at the Advanced Photon Source synchrotron at the Argonne National Laboratory (*29*). Sample pellets were placed inside a quartz in situ cell that was surrounded by a tube furnace for temperature control and connected to a gas manifold for controlling gas composition and flow. Further details concerning the beamline setup and sample preparation methods can be found in the Supporting Information. X-ray absorption near-edge structure (XANES) spectra of the passivated Co-Mn catalysts with Mn/Co atomic ratios of 0, 0.01, 0.05, 0.1, and 0.5 were measured at both the Mn K-edge (6539 eV) and Co K-edge (7709 eV) at ambient conditions. Reduction of the catalysts was then performed by heating the in situ cell at 4 K/min in flowing H_2 to 673 K, holding at 673 K for 2 h, and cooling to 493 K. XANES spectra of the reduced catalysts were then collected at 493 K at both the Mn and Co K-edges. Syngas (H_2:CO 2:1) was then introduced into the in situ cell, and the catalyst was aged for 6 h, which was determined by reaction experiments to be adequate for reaching a stable activity. XANES spectra of the catalysts under reaction conditions were then measured at both the Mn and Co K-edges. The XAS data were analyzed using the Demeter software family, which uses IFEFFIT internally (*30*) (*31*).

2.7 Infrared Spectroscopy

Fourier transform infrared spectroscopy (FTIR) measurements were made using a Thermo Scientific Nicolet 6700 FTIR spectrometer equipped with a liquid N_2-cooled MCT detector. Spectra were collected in transmission mode from 1200 cm^{-1} to 4000 cm^{-1} with 1 cm^{-1} resolution. For each spectrum, 32 scans were averaged to improve the signal-to-noise ratio. The catalyst samples were pressed into thin wafers and loaded into an in situ cell containing CaF_2 windows. The cell was flushed for 30 min with He flowing at 100 ml/min before reducing the catalyst at 623 K for 2 h in a 100 ml/min flow of H_2. Then, the cell was flushed with He while cooling to 493 K before introducing adsorbates. IR spectra were collected at different partial pressures of CO by adjusting the volumetric flow rates of CO and He diluent. Measurements in syngas were made with a 2:1 ratio of H_2 to CO. All spectra were collected at 493 K and 1 bar total pressure, and for a given condition, measurements were repeated until the spectra demonstrated negligible changes over 30 min. Control measurements were also made using blank silica and Mn on silica samples.

2.8 Catalytic Reactions

The activity and selectivity of the catalysts for Fischer-Tropsch synthesis were determined by carrying out reactions in a fixed-bed reactor. An Agilent 6890N gas chromatograph was used to measure the hydrocarbons, H_2, Ar, and CO in the reactor effluent. A full description of the reactor apparatus is provided in the Supporting Information. In a typical experiment, 50 mg of catalyst and 150 mg of calcined silica diluent were mixed together and loaded into the reactor. The catalyst was then heated at 4 K/min to at 673 K with flowing H_2. After holding at 673 K for 2 h, the reactor was cooled at 10 K/min to the desired reaction temperature while flushing He. The composition of the gas feed to the reactor was gradually switched from He to syngas over 10 min to prevent runaway conditions. For most experiments, the syngas had a 2:1 ratio of H_2 (Praxair, 99.999 % purity) to CO (Praxair, 99.9 % purity) with 7% Ar (Praxair, 99.999 % purity) included as an internal standard. Variations of reactant pressures were done by blending separate streams of H_2 and CO using calibrated mass flow controllers. The CO supply contained 20% Ar as an internal standard. The CO conversion was adjusted by changing the total gas flow rate through the reactor.

Before conducting the reaction experiments, the background activity of the empty reactor, silica support, and Mn deposited onto silica were all verified to be negligible. It was determined that internal transport limitations could be neglected at all operating conditions by means of the Weisz-Prater criterion (*32*). The absence of external transport limitations was verified by a series of exploratory measurements at different space velocities and bed loadings. As reported previously, conversion of the CO to hydrocarbons was calculated both on the basis of CO consumed and on the basis on hydrocarbons produced (*19*). The former allowed determination of the C_{5+} product selectivity without measuring the individual components of the liquid product fraction, while the latter proved to be more accurate at low conversions and operating conditions that led to negligible wax production. At all tested reaction conditions, the production of CO_2 was not detected and the selectivity toward oxygenates on a molar carbon basis was less than 1 %.

Catalytic activity for the Boudouard reaction, in which CO dissociates to form surface carbon and CO_2, was assessed by reducing a given catalyst in a quartz reactor and exposing the catalyst to CO at 493 K and 1 bar for a fixed time ranging from 15 min to 3 h. The reactor was then flushed with He at 673 K for 15 min to remove gas phase and molecularly adsorbed CO. The yield of dissociated CO was then determined by flushing the reactor with H_2 and monitoring the reactor effluent for methane using an MKS Minilab mass spectrometer. A makeup flow of He with a 1% Ar internal standard was present during the methanation to account for any changes in volumetric flow.

3. Results

3.1 Microscopy

To assess the size distributions of the Co nanoparticles within the catalysts, TEM images were acquired for each catalyst sample. Representative TEM images for the unpromoted, low Mn loading (Mn/Co = 0.1), and high Mn loading (Mn/Co = 0.5) catalysts are shown in Figure 1. For all levels of Mn loading, the nanoparticles were approximately spherical in shape and had particle sizes ranging from about 5 nm to 20 nm. The surface mean diameters, presented in Table 1, were close to 10 nm for all loadings; however, the standard deviation of the particle size distributions increased with higher Mn loadings. Elemental maps obtained via STEM-EDS were necessary for discriminating between Co and Mn in the catalyst samples. Figure 2 contains representative elemental maps for Mn/Co atomic ratios of 0, 0.01, 0.05, 0.1, and 0.5. In these images, the colors red, green, and blue correspond to the Mn, Co, and Si, respectively. The relative pixel intensities of the Co and Mn channels were scaled according to the total X-ray counts for each channel. A notable feature of the samples with Mn/Co atomic ratios of 0.01 and 0.05 was the absence of Mn-rich agglomerates. At a loading of Mn/Co = 0.1, the presence of Mn became apparent in the weighted elemental map, but there remained no evidence for separate, Mn-rich particles comparable in size to the Co nanoparticles. Only at a high loading of Mn/Co = 0.5 was there visual evidence for Mn-rich particles with diameters greater than several nanometers.

The compositions of individual nanoparticles were determined by selecting circular regions around a Co nanoparticle and any adjacent Mn in the STEM-EDS elemental maps. The X-ray counts for Co and Mn in each quantification region were totaled and converted to a Mn/Co atomic ratio. This process was repeated for over 100 nanoparticles in each sample to generate nanoparticle composition statistics for all Mn loadings, which are reported in Table 1. The average nanoparticle composition was almost identical to the bulk composition for the Mn/Co = 0.01 catalyst, but catalysts with higher promoter loadings exhibited average nanoparticle compositions substantially lower than the corresponding bulk compositions. Figure 3 shows histograms of the nanoparticle compositions and illustrates the broadening of the composition distribution with higher Mn loading. The shapes of the histograms are more evident in Supporting Information, Figure S1 in which the horizontal axes were rescaled to cover six standard deviations in the Mn/Co ratio. From these data, it is apparent that the distributions are modeled well by Gaussian functions, and that the distributions have similar relative standard deviations. These values were between 20 % and 25 % for the catalysts with bulk Mn/Co ratios of 0.01, 0.1, and 0.5. The Mn/Co = 0.01

catalyst had a higher relative standard deviation of 36 %, but this may have been due to the contribution of instrument error near the detection limit of STEM-EDS.

3.2 H_2 Chemisorption and O_2 Titration

The results from the static chemisorption experiments with H_2 are presented in Table 2. These data demonstrate that the total exposed surface area of the metallic Co nanoparticles decreased monotonically as the Mn loading increased. For the unpromoted catalyst, the mean particle size and dispersion determined by H_2 uptake were 12 nm and 8 %, respectively, which are in good agreement with the values determined by TEM imaging of 11 nm and 9 %. However, the H_2 uptake of the catalyst prepared with Mn/Co = 0.5 was about an order of magnitude less than that of the unpromoted catalyst, suggesting blockage of the Co surface by Mn species. Control samples of the silica support with and without Mn showed no evidence for H_2 chemisorption, which implies that all observed H_2 uptake was due to adsorption onto the surface of Co nanoparticles unless spillover from the Co onto the MnO_x were to occur. Although we cannot rule out the occurrence of spillover from the H_2 uptake data alone, this phenomenon seems unlikely given that the stoichiometric ratio of H to linearly adsorbed CO determined by CO TPD was about 1:1 for all Mn loadings.

O_2 uptake values from the O_2 titration experiments are also provided in Table 2. These data were used to calculate the extent of Co reduction as a function of Mn loading. These calculations account for pre-existing CoO and the co-oxidation of the promoter, which is often neglected in the literature and, if not corrected for, can lead to substantial overestimation of the Co extent of reduction at high Mn loadings. The oxidation states of the Mn and Co before and after the O_2 titrations were inferred from the XANES measurements and published phase diagrams (*33*). The data reveal that the fraction of Co in a metallic state following reduction decreased as Mn loading increased, which is consistent with reports of Mn impeding Co reduction (*34*).

3.3 X-ray Absorption Spectroscopy

Figure 4 displays the X-ray absorption spectra near the Co K-edge for the passivated and reduced Co-Mn catalysts at various Mn loadings. The edge energies of the passivated catalysts were located between those of the CoO and Co_3O_4 standards. Additionally, linear combination fits of the XANES regions were most consistent with the assumption that Co present in the passivated catalysts is a mixture of CoO and Co_3O_4. After reduction in H_2 at 673 K, the catalysts exhibited a shift in the Co edge toward lower energies closer to the edge of the Co(0) standard. The magnitude of this shift decreased with increasing Mn loading,

suggesting that the addition of Mn impeded the reduction of Co to the metallic state. Linear combination fitting of the Co XANES spectra revealed that the Co species in the reduced catalysts were a mixture of Co(0) and CoO. This analysis was also used to estimate the extent of Co reduction. The results listed in Table 3 indicate that the extent of Co reduction decreased with increasing Mn loading. Although the estimates of Co reduction from XANES are lower than the values determined by oxygen titration, the same influence of Mn loading on the Co reduction was observed by both methods. After exposure to syngas at 493 K for 6 h, the Co edges exhibited a small shift to lower energies, which suggests that several percent of the Co continued to reduce during the first 6 h of time-on-stream.

XANES data were collected at the Mn K-edge for all catalysts in a passivated state at ambient conditions and after reduction in H_2 at 673 K for 2 h. The reduced catalysts were then exposed to syngas at 493 K for 6 h and measured again. Data collected at the Mn K-edge for a representative catalyst with Mn/Co = 0.1 are presented in Figure 5. The XANES spectra shown in Figure 5A indicate that the edge energy for the passivated catalyst was located between those of the Mn_2O_3 and MnO_2 standards. After reduction, the catalyst Mn edge energy shifted to an energy close to that of the MnO standard. Exposing the catalyst to syngas did not cause major changes to the spectrum. A more quantitative approach for determining apparent oxidation states from XANES data involves constructing a linear relationship between oxidation state and the centroid of the 1s to 3d pre-edge feature (*35*). This method, depicted in Figure 5B for the catalyst with Mn/Co = 0.1, yielded the same conclusions as inspecting the edge energy shifts. The apparent Mn oxidation states for catalysts with various promoter loadings in the passivated state, reduced state, and under reaction are listed in Table 3. All loadings showed evidence of Mn being in an oxidized state between 2+ and 3+ after the reduction pretreatment step.

3.4 CO Temperature Programed Desorption

Several CO desorption peaks were observed in the TPD data for the Mn-promoted and unpromoted catalysts (Supporting Information, Figure S2A). In each run, a peak near 265 K was observed, which was attributed to physisorbed CO because the same peak appeared in control measurements done with the silica support. No additional CO desorption peaks were measured on either the silica or Mn deposited on silica control samples. The first chemisorbed CO peak on the catalyst samples occurred near 450 K, and higher temperature desorption peaks were observed between 600 to 700 K. Using the Redhead model (*36*) with an assumed pre-exponential factor of 10^{13} s^{-1}, the lower temperature peaks were calculated to correspond to CO with desorption activation energies near 95 kJ/mol and the more strongly bound CO had energies between 130 – 150 kJ/mol. The binding energy for the low-temperature peak falls within the

range of energies reported by multiple studies for linearly adsorbed CO at high CO surface coverages (*37*) (*38*). The literature on CO adsorbed at bridge sites is less extensive, but surface studies by Lahtinen et al. and Carlsson et al. assert that these species desorbed at lower temperatures than the linearly adsorbed CO (*39*) (*40*). This suggests that the signal from bridged CO species may be superimposed with the tail of the physisorbed CO peak. The high temperature desorption peaks have similarities to those observed by Bridge et al. of CO desorption from Co surfaces incorporating oxygen (*41*). Accordingly, it is proposed that these higher temperature peaks correspond to CO adsorbed in contact with the MnO promoter. Any peaks that may have occurred at temperatures higher than 723 K would have been obscured by dehydroxylation of the silica support.

As shown in Figure 6, the temperature of the first chemisorbed CO desorption peak maximum increased with higher Mn loading for Mn/Co atomic ratios between 0 and 0.1. A catalyst prepared with Mn/Co = 0.25 had a CO desorption temperature similar to that of the Mn/Co = 0.1 catalyst. Notably, these datapoints followed the same pattern as product selectivity: sensitivity to the promoter at low Mn loadings followed by a plateau for Mn/Co > 0.1. TPD experiments using catalysts prepared with Mn/Co ratios higher than 0.25 were not possible owing to the lower chemisorption uptake per g catalyst of these materials. The area ratios of the higher to lower temperature CO desorption peaks increased linearly with Mn loading (Supporting Information, Figure S2B), which indicates that a greater fraction of the CO adsorbate pool were bound in the more strongly interacting sites when Mn was present. By comparing the CO desorption peak areas to the H_2 static chemisorption uptakes, it was determined that the 1:1 CO:Co adsorption stoichiometry for sites corresponding to the lower temperature desorption peak was not affected by the presence of Mn. Overall, these findings are consistent with CO adsorbing both onto Co metal sites weakly affected by the Mn promoter and onto sites in direct contact with the MnO promoter and support.

3.5 Infrared Spectroscopy

In situ IR spectra revealed the presence of CO adsorbates on the catalyst surface when the reduced catalysts were exposed to CO at reaction temperature. In Figure 7A, the IR spectrum for the unpromoted catalyst shows a peak at 2077 cm^{-1} corresponding to linearly adsorbed CO (*42*). The Mn promoter induced a shift of this peak toward lower wavenumbers such that the Mn/Co = 0.5 catalyst had a peak position of 2068 cm^{-1}. Additionally, there was a slight increase in the peak area of bridging CO (1880-1890 cm^{-1}) relative to the linearly adsorbed CO as Mn loading increased. The most prominent difference between the spectra was the appearance of a peak at 1588 cm^{-1} when Mn was present.

Red-shifting of the linearly adsorbed CO peak is consistent with stronger binding of CO to the Co surface, but the connection of this feature to Mn remains ambiguous. In their study of ambient-temperature CO adsorption onto Mn-promoted Co catalysts, Morales et al. identified two linearly adsorbed CO peaks at 2030 cm^{-1} and 2050 cm^{-1} and found that higher Mn loading increased the prominence of the lower wavenumber peak relative to the higher wavenumber peak (*13*). Since the withdrawal of electron density from the Co by the MnO promoter would decrease π* back-donation to the adsorbed CO and hence increase the carbonyl stretch frequency, structural effects were suggested as the probable explanation for the differences between the unpromoted and Mn-promoted catalyst IR spectra. den Breejen et al. reported the same result for related catalysts (*15*). The catalyst preparation methods used in both studies resulted in smaller Co particles as Mn loading increased, which means that the findings could be a simple consequence of size effects. Smaller particles would also explain the lower intensity of bridging CO observed in the Mn-promoted catalysts, which differs from the findings of the present study. Catalysts with particle sizes close to 10 nm were used in the present study, which rules out Mn affecting CO adsorption through particle size effects alone, but it remains possible that the MnO promoter led to the formation of surface structures, possibly involving under-coordinated Co atoms, that resulted in CO adsorbates with comparatively weakened carbonyl bonds.

The peak at 1588 cm^{-1} is similar to those found in the IR spectra of various FTS catalysts, which have been attributed most frequently to carbonate species interacting with the catalyst support (*42*) (*43*). The absence of the peak from the unpromoted catalyst suggests these species were adsorbates interacting with the MnO and not the silica. Moreover, these adsorbates were not observed in the spectra for the MnO supported on silica control sample, suggesting that an interface between Co and MnOx was necessary for the appearance of these species. Given that the peak area scaled linearly with Mn loading, it is likely that this peak incorporated spillover of the CO onto the MnO rather than exclusively species at the Co-promoter interface. Nevertheless, this peak has a frequency similar those of carbonyl complexes in which separate metal atoms are bound to both the C and O atoms of the CO (*44*). By analogy to these complexes, it has been proposed for various heterogeneous catalyst systems that adsorbed CO may bind simultaneously to the metal and an oxophilic component of the promoter through the C and O atoms, respectively (*45*). With a vastly weakened carbonyl bond, such species would presumably undergo C–O dissociation much more readily than CO not at the interface with the metal oxide promoter.

To understand the relative reactivity of these species toward hydrogenation, IR spectra under transient conditions were collected for the catalyst prepared with Mn/Co = 0.1 as follows. The reduced catalyst was

exposed to flowing CO at 493 K to saturate the catalyst surface with carbonyl adsorbates, and then the flow through the in situ cell was switched to H_2 to start the hydrogenation of the adsorbed species. It was observed that the linearly adsorbed CO, bridging CO, and the species giving rise to the peak at 1588 cm^{-1} disappeared on the same timescale in the presence of H_2 (Figure S3). Additionally, a peak centered at 1619 cm^{-1} remained after 1 h exposure to H_2. Although not identifiable in the steady state spectra shown in Figure 7, this peak was present before starting the hydrogenation and its magnitude did not change significantly during the exposure to H_2. These results demonstrate that an inert carbonyl species associated with MnO_x forms on the promoted catalysts. However, there is also sufficient evidence to conclude that the IR peak at 1588 cm^{-1} is associated with a separate species that can undergo hydrogenation.

Flowing syngas over the reduced catalysts led to changes in the IR spectra as shown in Figure 7B. The co-presence of H_2 broadened and red-shifted the peaks corresponding to linearly adsorbed CO. These shifts were 13 cm^{-1} and 5 cm^{-1} for the unpromoted and Mn/Co = 0.5 catalysts, respectively. The red-shifting of the CO peak due to H_2 has been attributed to either repulsive interactions between co-adsorbed CO and H (*46*) or the contribution of electron density from the H to the Co metal that can increase the extent of π^* back-donation to the CO (*47*). The smaller magnitude of the shift in the Mn-promoted catalyst cannot be explained with certainty, but this effect may result from there being less H_2 adsorbed on the Mn-promoted catalysts. Interestingly, the intensity of the 1588 cm^{-1} peak relative to the linearly adsorbed CO peak for the Mn/Co = 0.5 catalyst did not change under syngas. However, a broad peak at the same frequency emerged in the spectrum for the unpromoted catalyst. Formate species have been suggested to form on FTS catalysts with vibrational frequencies between 1300 and 1600 cm^{-1} (*42*), which could account for this peak, but it cannot be determined whether the species exists on the Co metal or on the silica support. Peaks from C-H bonds (2855 cm^{-1}, 2927 cm^{-1}, and 2960 cm^{-1}) became visible when the catalyst was exposed to syngas. These peaks validate that hydrocarbons were forming on the catalyst surface during the measurements, but did not reveal any differences between the promoted and unpromoted catalysts. No discernable signal for CO_2 or for alcohol -OH groups was observed, which is consistent with the absence of alcohols in the product distributions observed in experiments conducted with packed-bed reactor.

3.6 Kinetics and Catalytic Performance

The dependencies of CO consumption rate on the partial pressures of H_2 and CO for the unpromoted, low Mn loaded (Mn/Co = 0.1), and high Mn loaded (Mn/Co = 0.5) catalysts at 493 K and extrapolated to 0 %

CO conversion are displayed in Figure 8. With fixed CO partial pressure, a linearly proportional relationship was found to exist between the rate and the partial pressure of H_2 for both catalysts (Figure 8A). Variation of the CO partial pressure with fixed H_2 partial pressure led to rate maxima being observed for both catalysts (Figure 8B). It was not possible to assign an unambiguous CO partial order dependence at CO partial pressures below which the rate maximum occurred owing to the narrow pressure range of this regime. However, at higher CO partial pressures beyond which the rate maximum occurred, the rate clearly exhibited a negative first order dependence on CO partial pressure, which is consistent with inhibition due to molecularly adsorbed CO. These data for both catalysts are consistent with the most commonly used rate law for describing FTS kinetics on Co-based catalysts, given as Eq. (3) (*48*). Here, r_{CO} is the rate of CO consumption, P_{CO} is the CO partial pressure, P_{H_2} is the H_2 partial pressure, and the parameter a is an apparent rate constant, and the parameter b is the CO adsorption constant. Although this Langmuir-Hinshelwood-type expression has its origins in empirical fitting, this rate law can be derived mathematically starting from the assumption of CO dissociation following a hydrogen-assisted pathway (*49*).

$$r_{CO} = \frac{abP_{CO}P_{H_2}}{(1+bP_{CO})^2} \quad (3)$$

CO consumption rates as a function of pressure for catalysts prepared with various Mn loadings are presented in Figure 9. These data were collected at 493 K using a 2:1 H_2:CO syngas composition with extrapolation to 0 % CO conversion. Figure 9A shows the data normalized by the weight loading of Co in each sample. Here, a Mn/Co atomic ratio of 0.01 increased the activity relative to that of the unpromoted catalyst by about 50 %. Higher loadings of promoter decreased the rate such that the Mn/Co = 0.05 catalyst had a specific activity similar to that of the unpromoted catalyst and the Mn/Co = 0.5 catalyst was about a factor of five less active than the unpromoted catalyst. When normalized by the number of Co atoms accessible to H_2 chemisorption (Figure 9B), the turnover frequency for CO consumption exhibited an increase with Mn/Co ratio. The one exception to this trend is the catalyst with Mn/Co = 0.5, which did not have the highest turnover frequency, but this could be an artifact of the high uncertainty of the H_2 uptake measurement for this catalyst.

All tested catalysts deactivated by about 30 % within the first several hours of time-on-stream. After this initial deactivation, the activities were stable to within 10 % over the course of the experiments, which lasted up to one week. Consequently, all reported data were collected after an initial 12 h aging period. Interestingly, no selectivity changes were detected within the aging period for any catalyst. This suggests

that the deactivation involved a decrease in the number of active sites rather than an alteration to the intrinsic activity of the sites. Such a phenomenon would lead to the turnover frequencies reported in Figure 9B being underestimated because the H_2 uptake measurements were performed using catalyst that had not been exposed to syngas. However, the qualitative conclusions from these data should not be affected because the percent deactivations of all catalysts after aging were similar.

Non-linear least squares regression was used to obtain parameters for the rate law, and these are listed in Table 4. The parameters a and b increased by factors of about 4 and 3, respectively, as the Mn/Co atomic ratio increased from 0 to 0.5. Kinetics data at various temperatures and pressures for each catalyst (Supporting Information, Figures S4 and S5) were collected in an attempt to extract estimates of pre-exponential factors and energies from the parameters a and b. This procedure required simultaneously fitting four parameters, and owing to cumulative error and the coupling between a and b that occurs as pressure increases, accurate estimates could not be obtained. However at high pressures, molecularly adsorbed CO becomes the most abundant surface species, and the rate law simplifies to Eq. (4) and an apparent rate constant equivalent to $\frac{a}{b}$ appears. The apparent pre-exponential factor and activation energy for this apparent rate constant calculated using kinetics data at 16 bar are reported in Table 4 as A_{app} and $E_{A,app}$, respectively. Parity plots showing the agreement between the experimental and predicted values are included in Supporting Information, Figure S6.

$$r_{CO} = \frac{aP_{H_2}}{bP_{CO}} \tag{4}$$

The effect of Mn promotion on CO disproportionation via the Boudouard reaction was investigated by exposing reduced catalysts to CO at 493 K and 1 bar. Although the concentration of CO_2 in the reactor effluent was not high enough to be measured reliably by online mass spectrometry, carbon on the catalyst surface was quantified by clearing the catalyst surface of adsorbed CO and then flushing H_2 through the reactor at 493 K to produce methane. The m/z = 16 signal was attributed to methane and not atomic O because the m/z = 15 signal, corresponding to CH_3 fragments, was proportional to the m/z = 16 signal. Moreover, the m/z = 16 signal was assumed to result from methanation of surface carbon rather than hydrogenation of undissociated CO because no increase in the m/z = 18 signal, corresponding to water, was observed when flushing the reactor with H_2. Figure 10 shows the quantity of methanated carbon normalized by the number of surface Co metal atoms as a function of CO exposure time for catalysts with different Mn loadings. A sample of 5 wt% MnO on silica did not yield any measurable methane signal even after 24 h of CO exposure. As seen by the trend of increasing slope through the data points with higher

Mn loading, the presence of Mn facilitated the CO disproportionation reaction. However for all catalysts, the CO disproportionation rates were about three orders of magnitude lower than the FTS turnover frequencies.

Dinse et al. demonstrated that at atmospheric pressure silica-supported catalysts have lower methane and higher C_{5+} selectivities when promoted with a Mn/Co atomic ratio close to 0.1 and that higher Mn/Co ratios lead to no further improvements to the product selectivity (*19*). However, the regime of Mn/Co ratios between 0 and 0.05 was not investigated in detail. In the present study, measurements of catalysts prepared by the same method but with lower loadings of promoter (Supporting Information, Figure S7) confirmed that Mn-induced improvements in the product selectivity reached a maximum at Mn/Co = 0.1. Moreover, this asymptotic trend of product selectivity as a function of Mn loading was confirmed to occur at high pressures (Figure 11). However, this optimal loading of Mn/Co = 0.1 should not be considered to be a universal optimum applicable for all catalyst synthesis methods. The extent to which an interface forms between the Co and MnO_x may vary depending on the materials and procedures used for catalyst preparation. This may account for the lack of an optimal promoter loading for silica-supported Co-Mn catalysts that were prepared using different pretreatment methods (*15*).

The disparity between the product selectivities of the unpromoted and Mn-promoted catalysts decreased with increasing pressure. At 1 bar, the unpromoted catalyst had a methane selectivity close to 40 %, whereas the catalyst for which Mn/Co = 0.1 had a methane selectivity of 20 %. At 16 bar, this performance difference decreased to less than 5% as the product distribution shifted to higher molecular weights for all catalysts. Additional selectivity data at various temperatures and pressures is included in Supporting Information, Figures S8, S9, and S10.

4. Discussion

4.1 Effects of Mn Promotion on Co Particle Size and Structure

The TEM images of the catalysts show that the inclusion of Mn in the catalyst formulation does not affect the mean diameters of the nanoparticles significantly. Consequently, it is unlikely that the changes to catalyst activity and selectivity observed upon Mn promotion are attributable to particle size effects. Moreover, the surface mean diameters were all close to 10 nm, and multiple researchers have reported that the turnover frequency for FTS on Co becomes insensitive to particle size above 6-10 nm (*50*) (*51*) (*52*). This reported phenomenon has been rationalized by the relative abundance of corner and edge sites to terrace sites as a function of particle size. The ratio of under-coordinated to terrace Co atoms reaches

a plateau at about 6 nm, assuming cuboctohedral nanoparticle geometry (*53*). Hence, it has been proposed that the terrace atoms are more active for FTS than the corner and edge atoms in a Co nanoparticle, and these under-coordinated sites possibly become poisoned by binding species too strongly (*54*). More recently, theoretical investigations by van Santen et al. have posited that lower CO dissociation barriers exist for Co sites at step-edges or on corrugated surfaces and that these sites may form in abundance only on nanoparticles above a certain size (*55*) (*56*). Prior studies on Co-Mn FTS catalysts have suggested that Mn can cause a decrease in the size of the Co nanoparticles formed relative to that of unpromoted Co (*13*) (*16*). These studies and our own previous work with Co-Mn catalysts reported that the size of Co nanoparticles decreases with increasing Mn content, based upon powder XRD line broadening measurements (*19*). We note, however, that such measurements may not yield an accurate measure of nanoparticle size owing to Mn-induced crystal defects in the Co nanoparticles, which would increase the prevalence of particles composed of several smaller domains.

Phase diagrams for bulk Co-Mn alloys indicate that at 673 K, the temperature used in this study for catalyst reduction, a transition from hexagonal close-packed (hcp) crystal structure to face-centered cubic (fcc) occurs in the region of low Mn/Co ratios where product selectivities are a strong function of promoter loading (*57*). Consequently, the possibility that the promotion effects were caused by a Mn-induced transition from hcp to fcc structure needs to be considered. XRD measurements of reduced catalyst samples sealed in inert gas revealed the presence of diffraction peaks corresponding to hcp Co metal in the unpromoted and Mn-promoted catalysts (Supporting Information, Figure S11 and Table S1). No peaks exclusively attributable to fcc Co metal or Mn oxides were detected. An analysis of the Co K-edge EXAFS data was not able to distinguish between these two Co metal crystal structures. In addition to this lack of experimental evidence for a crystal structure transition, there is consensus in the literature that runs counter to the hypothesis. It has been reported that the FTS turnover frequency of hcp Co nanoparticles is higher than that of fcc Co nanoparticles (*58*) (*59*). With regard to product selectivity, it is reported that either there is little difference in the product distribution for the two crystal structures or that fcc Co yields higher methane levels (*60*) (*61*). These findings lead to a prediction that a transition from the hcp to the fcc crystal structure would result in a decrease in site activity and possibly higher methane selectivity, which is contrary to what are the observed effects of Mn promotion.

4.2 Mn and Co Oxidation States

Co-Mn catalysts are invariably reported to have Mn in an oxidized state under FTS operating conditions. Studies by Tan et al. suggest that Mn forms MnO and Mn_2O_3 after catalyst reduction (*62*) (*63*). A series of

in situ XAS studies of Mn-promoted, titania-supported Co catalysts by Morales et al. have shown that the promoter adopts a 2+ oxidation state and that there is assortment of mixed oxides of Mn with the Co and Ti (*11*) (*64*) (*34*). These experiments provide a basis for invoking Mn oxide in rationalizing the promotion effects, but the quantity of promoter relative to Co in the catalysts studied by Morales et al. exceeded the threshold described in the present study at which catalyst performance became insensitive to Mn loading. High loadings of promoter that lead to the formation of spectator Mn oxide particles and the plethora of other Mn-containing species could obscure the signal from the Mn that is responsible for promotion effects. The rapid improvement followed by a plateau in the product selectivities as a function of Mn loading seen in the present study suggest that the state in which Mn exists up to a Mn/Co atomic ratio of 0.1 is vital for the observed promotion effects, whereas the Mn that accumulates at higher loadings effectively does not participate in the catalysis.

One hypothesis that was considered to explain the trends in catalyst performance as a function of promoter loading was the possible formation of an alloy of metallic Mn with Co on the nanoparticle surface, which may occur at the low Mn loadings where selectivity is highly sensitive to promoter loading. Since the surface free energy of Mn metal is much lower than that of Co, the Mn would be expected to locate preferentially on the nanoparticle surfaces (*65*). Furthermore, the Mn loading at which C_{5+} selectivity reaches a plateau is approximately equivalent to the amount necessary to form a monolayer on the nanoparticle surfaces (Mn/Co = 0.1). The saturation of the nanoparticle surfaces by Mn could explain why C_{5+} selectivity did not continue to improve beyond Mn/Co atomic ratios of 0.1. Although these trends are phenomenologically consistent, no evidence for metallic Mn was observed for the Co-Mn catalysts investigated in this study. XANES measurements at the Mn-edge revealed that a partial reduction of the Mn species occurred after reducing the catalysts in H_2 at 673 K. This is evident in both the shift of the Mn K-edge to lower energies upon reduction (Figure 5A) and the energy of the pre-edge features in the XANES spectra (Figure 5B). In the passivated catalyst, the apparent oxidation state of the Mn was closest to that of 4+ cations, and after reduction, the promoter formed species with a mixture of 2+ and 3+ cations. Consequently, Mn is likely present as an oxide for Mn/Co ratios below 0.1.

From the extents of reduction data, it is apparent that a portion of the Co in the unpromoted catalyst (~20%) remains unreduced, most likely as highly dispersed CoO or Co silicate. The presence of Mn also contributes to lower extents of Co reduction, suggesting that the MnO_x overlayer may incorporate Co to form Co-Mn mixed metal oxides. The Mn:Co stoichiometry of this mixed oxide cannot be quantified readily because it is unknown whether the Mn oxide affects Co silicate formation or inhibits the reduction

of the CoO nanoparticles without forming mixed metal oxides. If a portion of the Mn is dispersed over the support along with Co, this could account for the lower extent of Co reduction without being detectable by XRD, chemisorption, or microscopy.

4.3 Spatial Distribution of Mn

The absence of large agglomerates of MnO in the STEM-EDS images of the catalysts with Mn/Co atomic ratios of less than 0.1 (Figs. 2A and 2B) demonstrates that the promoter is finely dispersed over the Co. For this regime, it is also noted that the mean of the nanoparticle composition histogram for each catalyst sample is very close to the bulk Mn/Co ratio, and no nanoparticles in these catalysts have a Mn/Co ratio more than three standard deviations away from the value for the bulk catalyst. It can also be shown through material balance arguments that segregation of Mn away from the Co nanoparticles would result in Mn/Co ratios determined from STEM-EDS maps having an average value lower than the bulk catalyst composition. Hence, the close match between the compositions of the bulk and the individual nanoparticle is a reliable indicator of a preferential spatial association between the Mn and Co. From these findings, it can be inferred that an energetic interaction between the two metals exists which balances the entropic tendency of the promoter to disperse across the support, for which there is more surface area than on the Co nanoparticles.

Previous studies of Mn-promoted Co catalysts have reported that Mn accumulates selectively onto the Co nanoparticles. In their studies of titania-supported Co-Mn catalysts, Morales et al. found that although migration of the promoter onto the support occurred during catalyst pretreatment, MnO nanoparticles were visibly adjacent to Co nanoparticles in STEM-EELS images of the catalyst (*12*). Bezemer et al. have also reported contact between Co and Mn domains in reduced catalysts, although their catalysts were prepared with carbon nanofiber supports with which the MnO had limited chemical interaction (*14*). More recent studies by Feltes et al. (*16*) and Zhao et al. (*66*) have explored how preparing titania-supported Co-Mn catalysts by the strong electrostatic adsorption (SEA) method could enhance the spatial association between the two elements. It remains unclear how readily these findings can be translated to silica supports, especially given that these researchers found the Mn spatial distribution relative to the Co to be highly sensitive to changes in catalyst preparation methods. Moreover, these studies did not attempt to quantify the relative amount of Mn associated with individual Co nanoparticles.

At Mn/Co = 0.01, the average nanoparticle Mn/Co ratio is 0.0096, which is 96 % of the bulk catalyst composition. However, as Mn loading increases the discrepancy between the average nanoparticle

composition and the bulk composition grows. The average nanoparticle compositions for bulk Mn/Co ratios of 0.05, 0.1, and 0.5 are 92 %, 86 %, and 74 % of their respective bulk compositions. This trend indicates that spatial segregation between the Co nanoparticles and the Mn begins to occur as the Mn loading increases. This does not mean that less Mn is present near the Co nanoparticle surfaces in the catalysts with higher promoter loadings, but rather that the additional Mn in these catalysts has a tendency to accumulate separately from the Co nanoparticle surfaces. Evidence for this phenomenon is clearly seen by the presence of small Mn oxide particles in the elemental map of the catalyst for which Mn/Co = 0.5 (Figure 2D).

Evidence for coverage of the Co nanoparticle surfaces by Mn can be extracted from a comparison of the H_2 uptake data to the Co nanoparticle surface area determined from TEM particle size estimates and O_2 titration uptakes. Eq. (5) expresses how the fractional coverage of Co metal by Mn species was calculated using these data. To account for Co metal that was inaccessible to H_2 adsorption owing to nanoparticle contact with the silica support, the fraction of the nanoparticle surface covered by the silica support was included in the calculation via the parameter ε. Using the characterization data for the unpromoted catalyst, this correction factor was calculated according to Eq. (6) and determined to be 15 %. It is assumed that the fraction of the nanoparticle surface that was covered by silica is the same for each sample, which is a reasonable approximation given the similar Co nanoparticle sizes and shapes for all tested catalysts.

$$frac.\,Mn\ coverage = 1 - \frac{2(H_2\ uptake)}{(moles\ Co)(frac.\ Co\ reduced)(frac.\ dispersion)(1-\varepsilon)} \quad (5)$$

$$\varepsilon = 1 - \frac{2(H_2\ uptake)_{unpromoted}}{(moles\ Co)_{unpromoted}\,(frac.\ Co\ reduced)_{unpromoted}\,(frac.\ dispersion)_{unpromoted}} = 0.15 \quad (6)$$

The calculated percent surface coverages of Co nanoparticles by MnO reported in Table 2 indicate that higher Mn loadings lead to greater blockage of the Co metal surface. A Mn/Co atomic ratio of 0.01 results in only 9 % of the surface becoming inaccessible, and at a loading of Mn/Co = 0.5, 83 % of the nanoparticle surface is estimated to be covered by MnO species. At the loading where product selectivities become relatively insensitive to increasing Mn loading (Mn/Co = 0.1), the estimated Mn coverage is 48 %. These data do not reveal information about the perimeter between the Co metal and the islands of Mn oxide that decorated the nanoparticle surfaces. However, the coverage estimates are notable, considering that Williams et al. have reported through simulations that the perimeter between a surface and randomly deposited islands is maximized at approximately half a monolayer coverage (*67*). These trends between catalyst selectivity and surface coverage of the Mn over the Co nanoparticles support the hypothesis that Co active sites close to the interface with the Mn are responsible for the promotion effects.

4.4 Influence of Mn on the FTS Reaction and Surface Adsorbates

The agreement of the kinetics data with Eq. (3) suggests that FTS on the unpromoted and Mn-promoted catalysts follow reaction mechanisms that yield the same rate law. Although it cannot be inferred whether the same species appear in the sequence of elementary steps leading from CO and H_2 to the hydrocarbon products, the results are consistent with FTS proceeding by the H-assisted dissociation of CO for all catalysts. The principle effect of the Mn promoter on the rate law is through the magnitude of the parameters a and b in Eq. (3), which represent the apparent rate constant and CO adsorption constant, respectively. Increased values for these two parameters imply that Mn both facilitates the dissociation of CO, which is presumed to be the rate determining step for FTS, and increases the extent to which adsorbed CO covers the Co metal surface. Qualitatively, the impact of Mn on the parameter a manifests in the generally higher turnover frequencies for the promoted catalysts at a given pressure (Figure 9B); the decreased sensitivity of turnover frequency to pressure at higher Mn loadings (Figure 9B) illustrates the impact of Mn on the parameter b. The turnover frequencies increased nearly monotonically with Mn loading owing to the interplay between the apparent rate constant and the CO adsorption constant which appear in the numerator and denominator of the rate law given as Eq. (4), respectively. As Mn loading increased, the apparent activation energy, $E_{A,app}$, at 16 bar increased substantially (Table 4). However, the activation energy of the rate determining step could not be isolated because the apparent rate constant is a composite of several equilibrium constants along with the rate constant of the rate determining step. These circumstances preclude making meaningful inferences from the trend in the pre-exponential factors. The increase in $E_{A,app}$ with Mn loading could be due to larger CO heats of adsorption on the promoted catalysts, a phenomenon that is corroborated by the CO TPD and IR spectroscopy data, but this hypothesis remains speculative without information about the magnitudes of the other contributions to $E_{A,app}$.

With regard to product composition, the higher CO adsorption constant and apparent rate constant due to Mn promotion are consistent with the lower methane and higher C_{5+} selectivity of the promoted catalysts. A greater coverage of CO on the catalyst surface would decrease H availability, assuming competitive adsorption takes place between H_2 and CO, so as to favor chain growth at the expense of methanation and hydrogenation termination reactions. Moreover, a decrease in the abundance of vacant sites may impede the rate of alkyl chain termination to olefins through β-hydride abstraction. These changes in surface adsorbate abundances are also consistent with increased olefin to paraffin product ratios observable in the C_2-C_4 product fraction (*19*). Facilitated C–O bond cleavage would lead to the more

frequent appearance of C_1 monomers that could scavenge H to further promote chain growth over termination. Mn promotion led to selectivity improvements at all operating conditions although there were diminishing returns at high pressure. In general, Mn promotion had an impact on the FTS selectivity analogous to operating at a higher partial pressure of CO, which follows from the larger CO adsorption constant of the Mn-promoted catalysts. The selectivities for all catalysts converged as pressure increased, which is an expected outcome under the assumption that the differences in product selectivities among the catalysts were primarily due to differences in adsorbate coverages and that the CO surface coverage would reach saturation at high pressure. As previously reported (*19*), higher C_{5+} selectivities are obtainable with these catalysts at higher CO conversions, which highlights the importance of secondary reactions and water for tuning the product distribution.

The effects of Mn promotion on the FTS kinetics and selectivity are consistent with enhanced CO adsorption being an important contributor, and evidence for this trait was also observed in the experimental data that probed the surface adsorbates. Larger heats of adsorption on the Mn-promoted catalysts were seen by the shift of the linearly adsorbed CO TPD peak to higher temperatures and the relative growth of the higher temperature CO desorption peak at higher promoter loadings. The clustering of the desorption profile into two distinct desorption temperatures is an expected feature if there were a mix of "unpromoted" Co sites far from the interface with the promoter and "promoted" Co sites at these interfaces, respectively. From these data, it can be deduced that the higher temperature desorption peak cannot be solely from CO bound simultaneously to Co and MnO because the unpromoted catalyst also shows desorption at this temperature. Hence, the higher temperature peak may involve CO interacting with the silica support. Since the peak area scaled relatively linearly with the total quantity of the promoter, the peak also shows signs of spillover onto the MnO. It was observed during exploratory measurements that flowing undiluted syngas through a bed of freshly reduced catalyst resulted in a reactor temperature spike. This is expected if CO suddenly adsorbs onto the catalyst surface without sufficient time for the reactor to dissipate the released heat and remain isothermal. While this temperature spike was on the order of 10 K for the unpromoted catalyst, beds of the Mn-promoted catalyst with identical total Co metal surface area led to spikes of over 100 K. Although no quantitative reasoning can be done with these observations, these experimental curiosities are consistent with the CO heat of adsorption being higher when using Mn promoters.

The higher turnover frequencies and apparent rate constants on the promoted catalysts strongly suggest that CO dissociation is intrinsically faster on the Mn-promoted catalysts, but it must be conceded that

changes to H_2 adsorption or the equilibrium constants of intermediate steps could be confounding variables. CO disproportionation rates provide a simpler view of the ease by which CO dissociates on these catalyst, and these rates were found to increase with increasing Mn loading. This finding suggests that direct CO dissociation is facilitated by the presence of the promoter, which is consistent with the hypothesis that the promoter acts as Lewis acid to help break apart CO. Interestingly these observations are similar to those of Sachtler and Ichikawa, who found that the temperature at which CO_2 production was detectable decreased on Rh catalysts that had been promoted with Mn oxide (*23*).

4.5 Origin of Mn Promotion Effects

Given the absence of MnO_x peaks in the XRD spectra and the lack of visible MnO particles at low promoter loadings (Mn/Co ≤ 0.1), MnO_x is presumed to be highly dispersed over the surface of the Co nanoparticles, resulting in a large fraction of the surface Co atoms being in contact with the promoter. The proposed formation of a finely dispersed MnOx oxide overlayer for Mn/Co ratios less than 0.1 followed by the appearance of larger, segregated Mn oxide particles at higher loadings mirrors the onset of promotion effects at low promoter loadings followed by insensitivity of the product selectivity to promoter loading at Mn/Co ratios greater than 0.1. A conceptual framework for connecting these phenomena starts with the hypothesis that the interface between the Co metal and the Mn oxide promoter is responsible for the observed promotion effects.

As depicted in Figure 12, the Co metal sites can be partitioned into two ensembles: unpromoted sites that are not close to MnO (blue) and promoted sites that are adjacent to MnO (red). For a catalyst without any Mn promoter, the surface of a Co nanoparticle consists entirely of unpromoted sites, which is indicated by the blue shell surrounding the Co nanoparticle in Figure 12A. A small loading of promoter (Figure 12B, Mn/Co = 0.01) results in some surface Co atoms becoming adjacent to the MnO_x as shown by the sites that are highlighted in red. Although these sites are proposed to have improved activity and selectivity, the unpromoted sites are much more abundant so the catalyst with Mn/Co = 0.01 performs only marginally better than the unpromoted catalyst. As the promoter loading increases, the ratio of promoted to unpromoted Co sites should increase provided the promoter is well-distributed over the Co surface so as to form abundant interface sites. Accordingly, the product selectivity of the catalyst should improve with higher Mn loading until the fraction of sites that are promoted begins to dominate as depicted in Figs. 12C and 12D. Once the fraction of sites that are promoted approaches unity (Mn/Co = 0.1), further addition of promoter to the catalyst would begin to cover up the Co surface such that CO consumption

rates per gram Co would decrease simply by there being fewer active sites. This is depicted in Figure 12E for the catalyst with Mn/Co = 0.5 where larger patches of MnO_x cover the catalyst surface.

Previous studies have conjectured that the CO might bind to metal oxides through the O atom while being simultaneously bound to the metal through the C atom. In this scheme, the Mn would act as a Lewis acid drawing electron density from the O atom of the adsorbed CO (Supporting Information, Scheme S2). If CO dissociation occurred at such a site, the Mn may participate in a redox reaction whereby the Mn cation accepts the O atom and subsequently undergoes a reduction to regenerate the active site, which is a mechanism that has been proposed for rare earth oxide promoters (*68*). However, the first order rate dependence on H_2 suggests that direct CO dissociation moderated by Mn^{2+} is not the primary pathway by which dissociation of the C–O bond occurs under typical FTS conditions. Further supporting this conclusion is the observation that the rate of C deposition via CO disproportionation in the absence of H_2 occurs at a rate that is 10^3 slower than the rate of FTS at the same temperature. Therefore, we propose that MnO dispersed on the surface of Co weakens the C–O bond, but C–O bond dissociation does not occur until the CO molecule is partially hydrogenated.

5. Conclusions

By combining detailed kinetics data with nanoscale characterization methods, new relationships between catalyst structure and performance can be determined for Mn-promoted Co-based FTS catalysts. The inclusion of Mn in the catalyst formulation did not lead to significant changes in Co particle size or crystal structure, which suggests the role of the promoter was more than structural. Particle composition distributions obtained from quantitative STEM-EDS analysis revealed evidence for the preferential spatial association between Mn and Co and that Mn was finely dispersed over the Co nanoparticles at low catalyst Mn/Co ratios. At higher promoter loadings, larger Mn oxide particles formed, which did not influence the catalysis apart from decreasing the fraction of exposed Co metal surface area. These structural trends closely matched the dependence of product selectivity on the catalyst Mn/Co ratio. Notably, the Mn loading yielding the least methane and most C_{5+} was close to the half monolayer promoter loading that would be expected to maximize the number of Co metal surface sites in contact with the MnO promoter. These findings were consistent with the hypothesis that sites along the interface between Co and Mn were responsible for the promotion effects.

Active sites with altered affinity for CO adsorption and FTS reactivity were observed in the Mn-promoted catalysts. Signs of enhanced CO adsorption on Mn-promoted catalysts were observed via the higher CO

desorption temperatures and larger CO adsorption constant inferred from fitting the FTS kinetics data. Additionally, in situ infrared spectroscopy experiments revealed that the Mn-promoted catalysts have a relative abundance of CO adsorbates with weakened carbonyl stretch energies compared to the unpromoted catalyst. Although the extent to which these adsorbates participate in the FTS reaction remains unclear, these characterization data are consistent with the larger FTS apparent rate constant and the higher CO disproportionation activity observed with the Mn-promoted catalysts. Higher CO surface coverage and facilitation of CO dissociation are also qualitatively consistent with a heavier hydrocarbon product distribution owning to less H availability for methanation and paraffin chain termination as well as more rapid C_1 monomer generation. Mn promotion led to higher FTS turnover frequencies although the cobalt-time yields decreased with increasing Mn loading because the promoter covered an increasing fraction of the Co surface. These findings demonstrate that an optimally promoted catalyst requires a Mn loading that balances the maximization of the interface between Co metal and MnO with the avoidance of blockage of the Co active sites by MnO.

Supporting Information

Supporting information available: nanoparticle composition histograms, XRD patterns, activity parity plots, FTIR data, CO TPD data, catalytic performance data, and depictions of the hypothesized Co-Mn nanoparticle structures. This material is available free of charge via the Internet at http://pubs.acs.org.

Acknowledgments

This work was funded by the BP XC^2 program. Work at the Molecular Foundry was supported by the Office of Science, Office of Basic Energy Sciences, of the U.S. Department of Energy under Contract No. DE-AC02-05CH11231. This research used resources of the Advanced Photon Source, a U.S. Department of Energy (DOE) Office of Science User Facility operated for the DOE Office of Science by Argonne National Laboratory under Contract No. DE-AC02-06CH11357. We are grateful for discussions and TEM instrument training provided by Dr. Karen C. Bustillo. We acknowledge assistance with the XAS experiments from Dr. John Katsoudas, Dr. Joshua Wright, Dr. Andrew “Bean” Getsoian, Dr. Konstantinos Goulas, John Howell, Christopher Ho, and Alice Yeh. Furthermore, we acknowledge Dr. Konstantinos Goulas for collecting the CO TPD data presented in this work.

References

1. Zhang, Q.; Kang, J.; Wang, Y. *ChemCatChem* **2010,** 2, 1030-1058.
2. Khodakov, A. Y.; Chu, W.; Fongarland, P. *Chem. Rev.* **2007,** 107, 1692-1744.
3. Diehl, F.; Khodakov, A. Y. *Oil Gas Sci. Technol.* **2009,** 64, 11-24.
4. Chu, W.; Chernavskii, P. A.; Gengembre, L.; Pankina, G. A.; Fongarland, P.; Khodakov, A. Y. *J. Catal.* **2007,** 252, 215-230.
5. Adachi, M.; Yoshii, K.; Han, Y. Z.; Fujimoto, K. *Bull. Chem. Soc. Jpn.* **1996,** 69, 1509-1516.
6. Huber, G. W.; Butala, S. J. M.; Lee, M. L.; Bartholomew, C. H. *Catal. Lett.* **2001,** 74, 45-48.
7. Moradi, G. R.; Basir, M. M.; Taeb, A.; Kiennemann, A. *Catal. Commun.* **2003,** 4, 27-32.
8. Varma, R. L.; Dan-Chu, L.; Mathews, J. F.; Bakhshi, N. N. *Can. J. Chem. Eng.* **1985,** 63, 72-80.
9. Colley, S.; Copperthwaite, R. G.; Hutchings, G. J.; van der Riet, M. *Ind. Eng. Chem. Res.* **1988,** 27, 1339-1344.
10. Hutchings, G. J.; van der Riet, M.; Hunter, R. *J. Chem. Soc. Farad. T. 1* **1989,** 85, 2875-2890.
11. Morales, F.; de Groot, F. M. F.; Glatzel, P.; Kleimenov, E.; Hendrik, B.; Hävecker, M.; Knop-Gericke, A.; Weckhuysen, B. M. *J. Phys. Chem. B* **2004,** 108, 16201-16207.
12. Morales, F.; de Groot, F. M. F.; Gijzeman, O. L. J.; Mens, A.; Stephan, O.; Weckhuysen, B. M. *J. Catal.* **2005,** 230, 301-308.
13. Morales, F.; de Smit, E.; de Groot, F. M. F.; Visser, T.; Weckhuysen, B. M. *J. Catal.* **2007,** 246, 91-99.
14. Bezemer, G. L.; Radstake, P. B.; Falke, U.; Oosterbeek, H.; Kuipers, H. P. C. E.; van Dillen, A. J.; de Jong, K. P. *J. Catal.* **2006,** 237, 152-161.
15. den Breejen, J. P.; Frey, A. M.; Yang, J.; Holmen, A.; van Schooneveld, M. M.; de Groot, F. M. F.; Stephan, O.; Bitter, J. H.; de Jong, K. P. *Top. Catal.* **2011,** 54, 768-777.
16. Feltes, T. E.; Espinosa-Alonso, L.; de Smit, E.; D'Souza, L.; Meyer, R. J. *J. Catal.* **2010,** 270, 95-102.
17. Feltes, T. E.; Zhao, Y.; Klie, R. F.; Meyer, R. J.; Regalbuto, J. R. *ChemCatChem* **2010,** 2, 1065-1068.

18. Johnson, G. R.; Werner, S.; Bustillo, K. C.; Ercius, P.; Kisielowski, C.; Bell, A. T. *J. Catal.* **2015,** 328, 111-122.

19. Dinse, A.; Aigner, M.; Ulbrich, M.; Johnson, G. R.; Bell, A. T. *Journal of Catalysis* **2012,** 288, 104-114.

20. Atashi, H.; Siami, F.; Mirzaei, A. A.; Sarkari, M. *J. Ind. Eng. Chem.* **2010,** 16, 952-961.

21. Thiessen, J.; Rose, A.; Meyer, J.; Jess, A.; Curulla-Ferré. *Micropor. Mesopor. Mat.* **2012,** 164, 199-206.

22. Mansouri, M.; Atashi, H.; Tabrizi, F. F.; Mirzaei, A. A.; Mansouri, G. *J. Ind. Eng. Chem.* **2013,** 19, 1177-1183.

23. Sachtler, W. M.; Ichikawa, M. *J. Phys. Chem.* **1986,** 90, 4752-4758.

24. Boffa, A. B.; Lin, C.; Bell, A. T.; Somorjai, G. A. *Catal. Lett.* **1994,** 27, 243-249.

25. Guerrero-Ruiz, A.; Sepúlveda-Escribano, A.; Rodríguez-Ramos, I. *Appl. Catal. A-Gen.* **1994,** 120, 71-83.

26. Datye, A. K.; Xu, Q.; Kharas, K. C.; McCarty, J. M. *Catal. Today* **2006,** 111, 59-67.

27. Reuel, R. C.; Bartholomew, C. H. *J. Catal.* **1984,** 85, 63-77.

28. Bartholomew, C. H. *Catal. Lett.* **1990,** 7, 27-52.

29. Kropf, A. J.; Katsoudas, J.; Chattopadhyay, S.; Shibata, T.; Lang, E. A.; Zyryanov, V. N.; Ravel, B.; McIvor, K.; Kemner, K. M.; Scheckel, K. G.; Bare, S. R.; Terry, J.; Kelley, S. D.; Bunker, B. A.; Segre, C. U. *AIP Conference Proceedings*, 2010.

30. Ravel, B.; Newville, M. *J. Synchrotron Rad.* **2005,** 12, 537-541.

31. Newville, M. *J. Synchrotron Rad.* **2001,** 8, 96-100.

32. Weisz, P. B.; Prater, C. D. *Adv. Catal.* **1954,** 6, 143-196.

33. Yankin, A. M.; Balakirev, V. F. *Inorg. Mater.* **2002,** 38, 391-402.

34. Morales, F.; Grandjean, D.; Mens, A.; de Groot, F. M. F.; Weckhuysen, B. M. *J. Phys. Chem. B* **2006,** 110, 8626-8639.

35. Chalmin, E.; Farges, F.; Brown Jr., G. E. *Contrib. Mineral. Petrol.* **2009,** 157, 111-126.

36. Redhead, P. A. *Vacuum* **1962,** 12, 203-211.

37. Couble, J.; Bianchi, D. *Appl. Catal. A-Gen.* **2012,** 445-446, 1-13.

38. Patanou, E.; Tveten, E. Z.; Chen, D.; Holmen, A.; Blekkan, E. A. *Catal. Today* **2013,** 214, 19-24.

39. Lahtinen, J.; Vaari, J.; Kauraala, K. *Surf. Sci.* **1998,** 418, 502-510.

40. Carlsson, A. F.; Naschitzki, M.; Bäumer, M.; Freund, H.-J. *J. Phys. Chem. B* **2003,** 107, 778-785.

41. Bridge, M. E.; Comrie, C. M.; Lambert, R. M. *Surf. Sci.* **1977,** 67, 393-404.

42. Fredriksen, G. R.; Blekkan, E. A.; Schanke, D.; Holmen, A. *Chem. Eng. Technol.* **1995,** 18, 125-131.

43. Liao, L. F.; Lien, C. F.; Shieh, D. L.; Chen, M. T.; Lin, J. L. *J. Phys. Chem. B* **2002,** 106, 11240-11245.

44. Sachtler, W. M. H.; Shriver, D. F.; Hollenberg, W. B.; Lang, A. F. *J. Catal.* **1985,** 92, 429-431.

45. Nonneman, L. E. Y.; Ponec, V. *Catal. Lett.* **1990,** 7, 197-204.

46. Beitel, G. A.; de Groot, C. P. M.; Oosterbeek, H.; Wilson, J. H. *J. Phys. Chem. B* **1997,** 101, 4035-4043.

47. Sato, K.; Inque, Y.; Kojima, I.; Miyazaki, E.; Yasumori, I. *J. Che. Soc. Faraday Trans. 1* **1984,** 80, 841-850.

48. Yates, I. C.; Satterfield, C. N. *Energ. Fuel* **1991,** 5, 168-173.

49. Ojeda, M.; Nabar, R.; Nilekar, A. U.; Ishikawa, A.; Mavrikakis, M.; Iglesia, E. *J. Catal.* **2010,** 272, 287-297.

50. Iglesia, E. *Appl. Catal. A* **1997,** 161, 59-78.

51. Bezemer, G. L.; Bitter, J. H.; Kuipers, H. P. C. E.; Oosterbeek, H.; Holewijn, J. E.; Xu, X.; Kapteijn, F.; van Dillen, A. J.; de Jong, K. P. *J. Am. Chem. Soc.* **2006,** 128, 3956-3964.

52. Zeng, B.; Hou, B.; Jia, L.; Wang, J.; Chen, C.; Sun, Y.; Li, D. *ChemCatChem* **2003,** 5, 3794-3801.

53. Umpierre, A. P.; de Jesús, E.; Dupont, J. *ChemCatChem* **2011,** 3, 1413-1418.

54. den Breejen, J. P.; Radstake, P. B.; Bezemer, G. L.; Bitter, J. H.; Frøseth, V.; Holmen, A.; de Jong, K. P. *J. Am. Chem. Soc.* **2009,** 131, 7197-7203.

55. van Santen, R. A.; Ghouri, M. M.; Shetty, S.; Hensen, E. M. H. *Catal. Sci. Technol.* **2011,** 1, 891-911.

56. Joos, L.; Filot, I. A. W.; Cottenier, S.; Hensen, E. J. M.; Waroquier, M.; Speybroeck, V. V.; van Santen, R. A. *J. Phys. Chem. C* **2014,** 118, 5317-5327.

57. Ishida, K.; Nishizawa, T. *Bull. Alloy Phase Diagr.* **1990,** 11, 125-137.

58. Enache, D. I.; Rebours, B.; Roy-Auberger, M.; Revel, R. *J. Catal.* **2002,** 205, 346-353.

59. Sadeqzadeh, M.; Karaca, H.; Safonova, O. V.; Fongarland, P.; Chambrey, S.; Roussel, P.; Griboval-Constant, A.; Lacroix, M.; Curulla-Ferré, D.; Luck, F.; Khodakov, A. Y. *Catal. Today* **2001,** 164, 62-67.

60. Ducreux, O.; Rebours, B.; Lynch, J.; Roy-Auberger, M.; Bazin, D. *Oil Gas Sci. Technol.* **2009,** 64, 49-62.

61. Gnanamani, M. K.; Jacobs, G.; Shafer, W. D.; Davis, B. H. *Catal. Today* **2013,** 215, 13-17.

62. Tan, B. J.; Klabunde, K. J.; Tanaka, T.; Kanai, H.; Yoshida, S. *J. Am. Chem. Soc.* **1988,** 110, 5951-5958.

63. Tan, B. J.; Klabunde, K. J.; Sherwood, P. M. A. *J. Am. Chem. Soc.* **1991,** 855-861, 113.

64. Morales, F.; Grandjean, D.; de Groot, F. M. F.; Stephan Odile; Weckhuysen, B. M. *Phys. Chem. Chem. Phys.* **2005,** 7, 568-572.

65. Tyson, W. R.; Miller, W. A. *Surf. Sci.* **1977,** 62, 267-276.

66. Zhao, Y.; Feltes, T. E.; Regalbuto, J. R.; Meyer, R. J.; Klie, R. F. *Catal. Lett.* **2011,** 141, 641-648.

67. Williams, K. J.; Boffa, A. B.; Lahtinen, J.; Salmeron, M.; Bell, A. T.; Somorjai, G. A. *Catal. Lett.* **1990,** 5, 385-394.

68. Barrault, J.; Guilleminot, A. *Appl. Catal.* **1986,** 21, 307-312.

69. Cliff, G.; Lorimer, G. W. *J. Microsc.* **1975,** 103, 203-207.

70. Perkins, Jr., G.; Laramy, R. E.; Lively, L. D. *Anal. Chem.* **1963,** 35, 360-362.

Table 1. Microscopy characterization data for the Co-Mn catalysts. The average Mn/Co ratios of the nanoparticles within the catalysts were determined by quantifying the composition of individual nanoparticles observed in the STEM-EDS elemental maps. Particle diameters were determined using TEM images assuming a site density of 14.6 Co atoms/nm^2 for supported nanoparticles (*27*).

Bulk Mn/Co Ratio	Avg. Particle Mn/Co Ratio	d(Co)[a] (nm)	Dispersion[b] (%)
0.00	–	11 ± 2	9 ± 2
0.01	0.001 ± 0.003	10 ± 2	10 ± 2
0.05	0.05 ± 0.01	10 ± 3	10 ± 3
0.10	0.09 ± 0.02	10 ± 3	9 ± 3
0.50	0.4 ± 0.1	12 ± 4	8 ± 3

[a] surface mean diameter

[b] based on TEM particle size

Table 2. H_2 chemisorption and O_2 titration characterization data for the Co-Mn catalysts. H_2 uptakes per gram catalyst were determined by static chemisorption. O_2 uptakes per gram catalyst were measured by pulse titration of the reduced catalysts with 10% O_2 in He. The extents of reduction were calculated assuming that the catalysts initially consisted of a mixture of Co(0), CoO, and MnO and that full oxidation of Co and CoO to Co_3O_4 and Mn to MnO_2 occurred. The coverages of the Co nanoparticle surfaces by MnO were estimated according to Eq. (5) using the H_2 uptake data and TEM dispersions (Table 1).

Bulk Mn/Co Ratio	H_2 Uptake (mmol g^{-1})	O_2 Uptake (mmol g^{-1})	Co(0)[a] (%)	MnO Coverage[b] (%)
0.00	0.051 ± 0.006	0.93 ± 0.04	79 ± 5	–
0.01	0.045 ± 0.005	0.89 ± 0.03	74 ± 4	10 ± 20
0.05	0.032 ± 0.007	0.91 ± 0.05	76 ± 6	40 ± 20
0.10	0.021 ± 0.005	0.86 ± 0.04	64 ± 5	50 ± 20
0.50	0.005 ± 0.002	1.01 ± 0.06	58 ± 8	80 ± 10

[a] percentage of Co in the metallic state after pretreatment

[b] estimate of the percentage of the total metallic Co nanoparticle surface covered by MnO

Table 3. Oxidation state data from XAS measurements for the Co-Mn catalysts. The extents of Co reduction were estimated by linear combination fitting of the Co K-edge XANES spectra using the spectra of Co foil, CoO, and Co_3O_4 as references. The apparent oxidation states of Mn were estimated by the position of the pre-edge feature in the Mn K-edge spectra.

Bulk Mn/Co Ratio	Co(0)[a] (%)	Passivated Mn Oxidation State	Reduced Mn Oxidation State	FTS Reaction Mn Oxidation State
0.00	55	–	–	–
0.01	51	4.2	2.5	2.0
0.05	43	4.5	2.2	2.0
0.10	28	4.2	2.2	2.5
0.50	23	4.5	2.7	2.7

[a] percentage of Co in the metallic state after pretreatment

Table 4. Kinetic parameters for the Co-Mn catalysts. The parameters *a* and *b* correspond to those in the rate law given as Eq. (3). The apparent pre-exponential factors and activation energies were calculated using kinetics data at 16 bar where the rate law simplifies to Eq. (4).

Bulk Mn/Co Ratio	*a* at 493 K ($bar^{-1}s^{-1}$)	*b* at 493 K (bar^{-1})	A_{app} ($bar^{-1}s^{-1}$)	$E_{A,app}$ (kJ/mol)
0.00	0.071	1.6	1×10^{8}	88
0.01	0.11	1.7	6×10^{9}	101
0.05	0.10	2.1	1×10^{13}	134
0.10	0.17	3.6	4×10^{15}	157
0.50	0.30	4.6	2×10^{16}	163

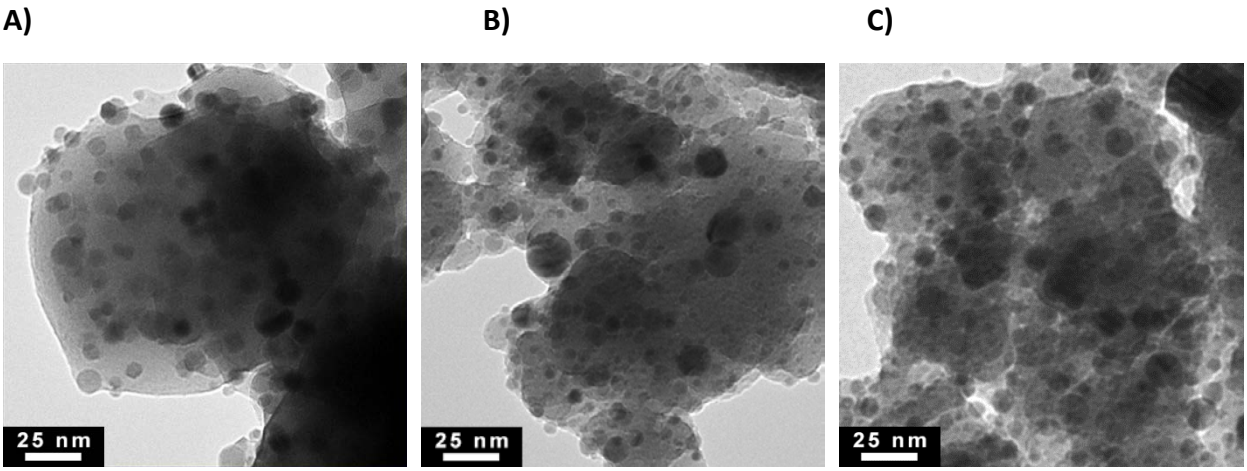

Figure 1. Bright-field TEM images of Co-Mn catalysts with bulk Mn/Co atomic ratios of (A) Mn/Co = 0, (B) Mn/Co = 0.1, and (C) Mn/Co = 0.5. For all catalysts, the Co loadings were 10 wt% relative to Co and silica. Particle size distribution statistics are reported in Table 1.

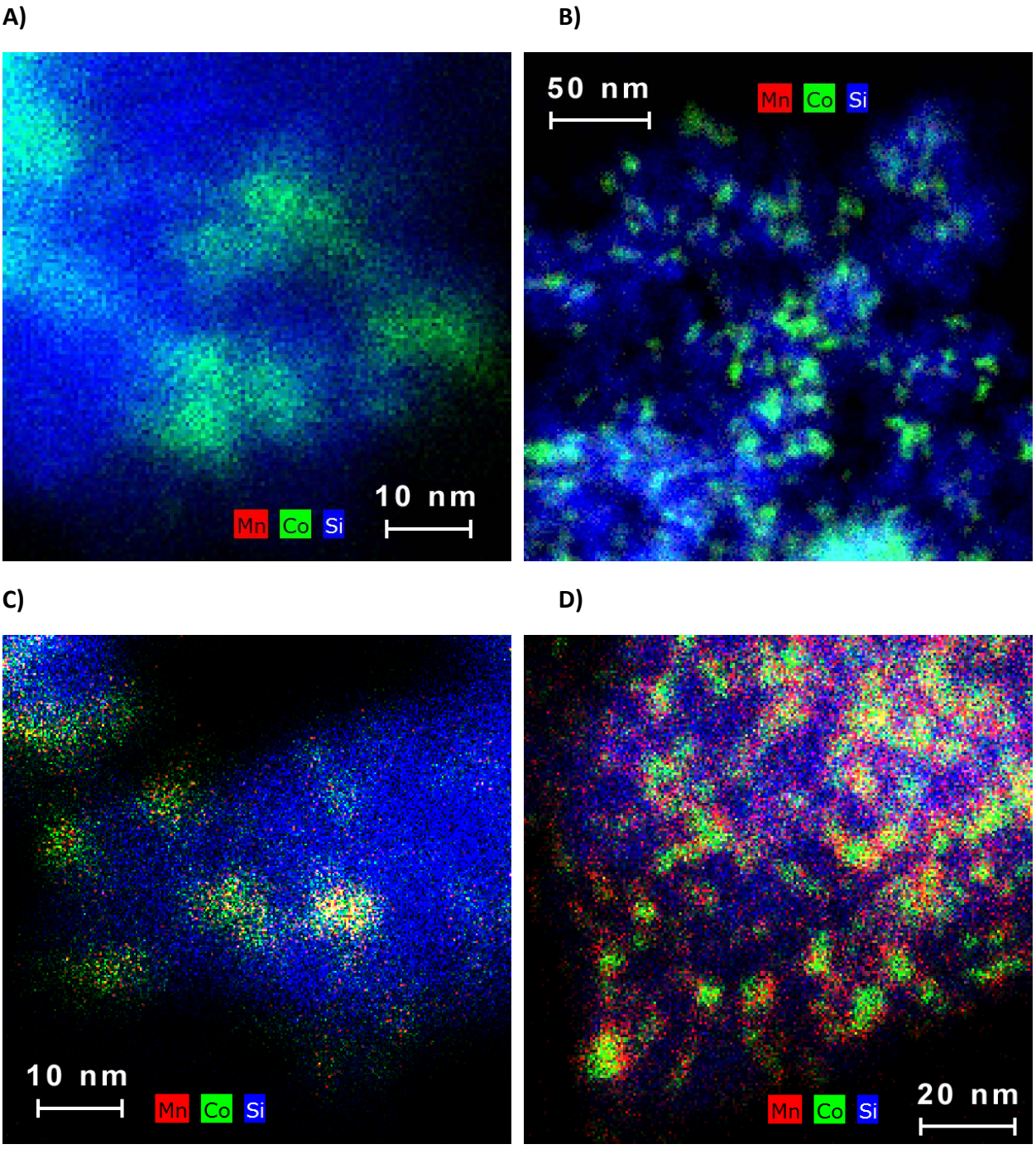

Figure 2. STEM-EDS elemental maps of Co-Mn catalysts with bulk Mn/Co atomic ratios of (A) Mn/Co = 0.01, (B) Mn/Co = 0.05, (C) Mn/Co = 0.1, and (D) Mn/Co = 0.5.

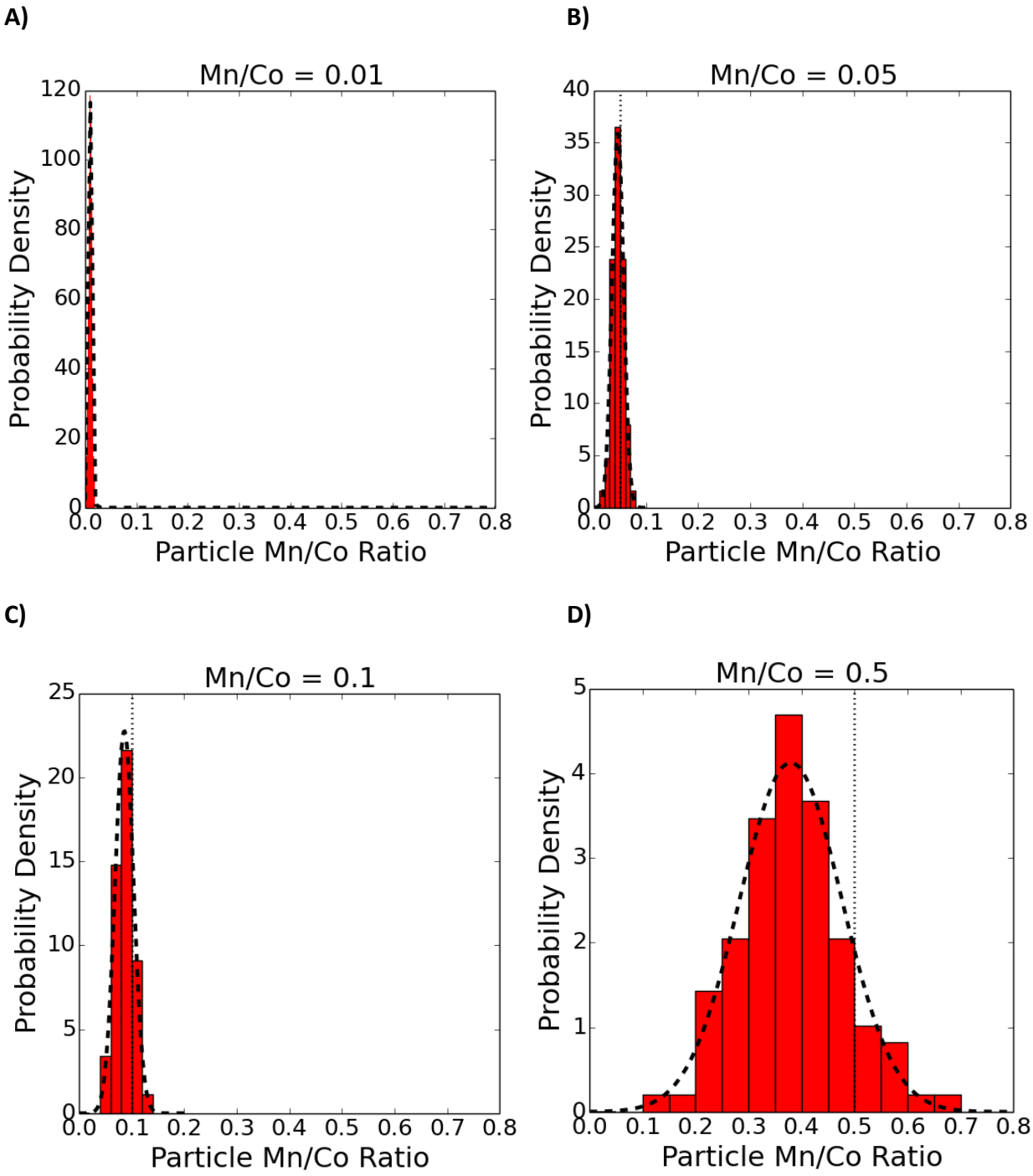

Figure 3. Histograms of Co-Mn nanoparticle compositions for bulk Mn/Co atomic ratios of (A) 0.01, (B) 0.05, (C) 0.1, and (D) 0.5. The dashed curve in each plot is a Gaussian function fitted to the data, and the vertical dotted line indicates the bulk catalyst composition.

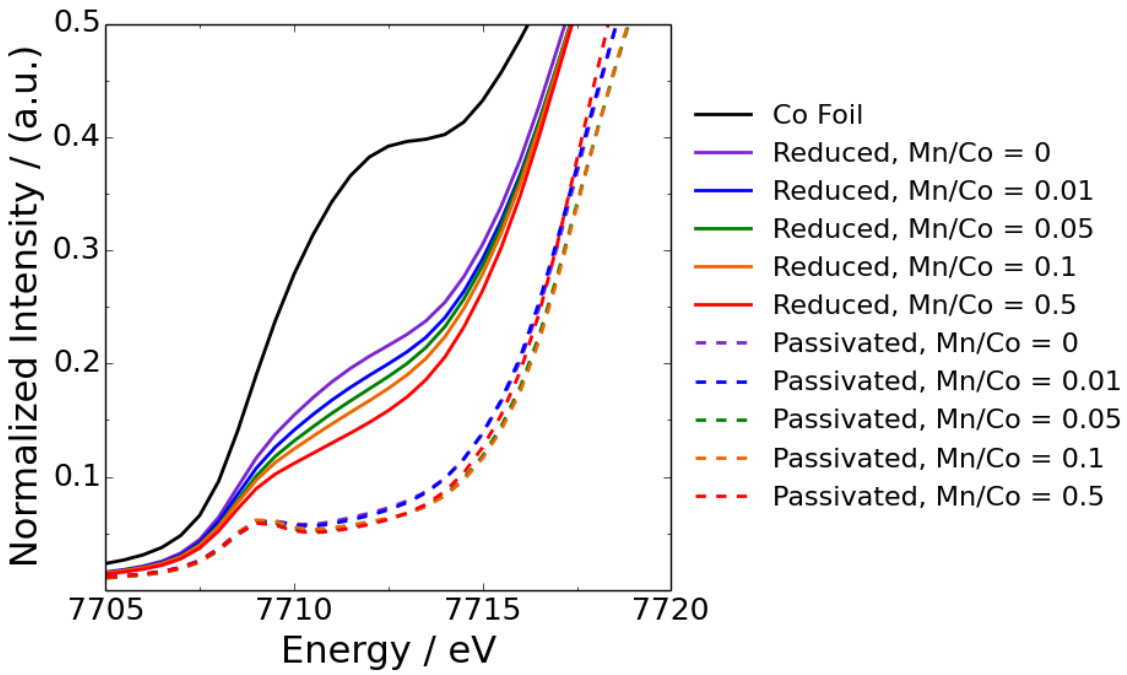

Figure 4. XANES spectra at the Co K-edge for the Co-Mn catalysts. After collecting the spectra for the catalysts in a passivated state at ambient conditions, the samples were reduced at 673 K in H_2 for 2 h. Spectra were then collected for the catalysts in the reduced state.

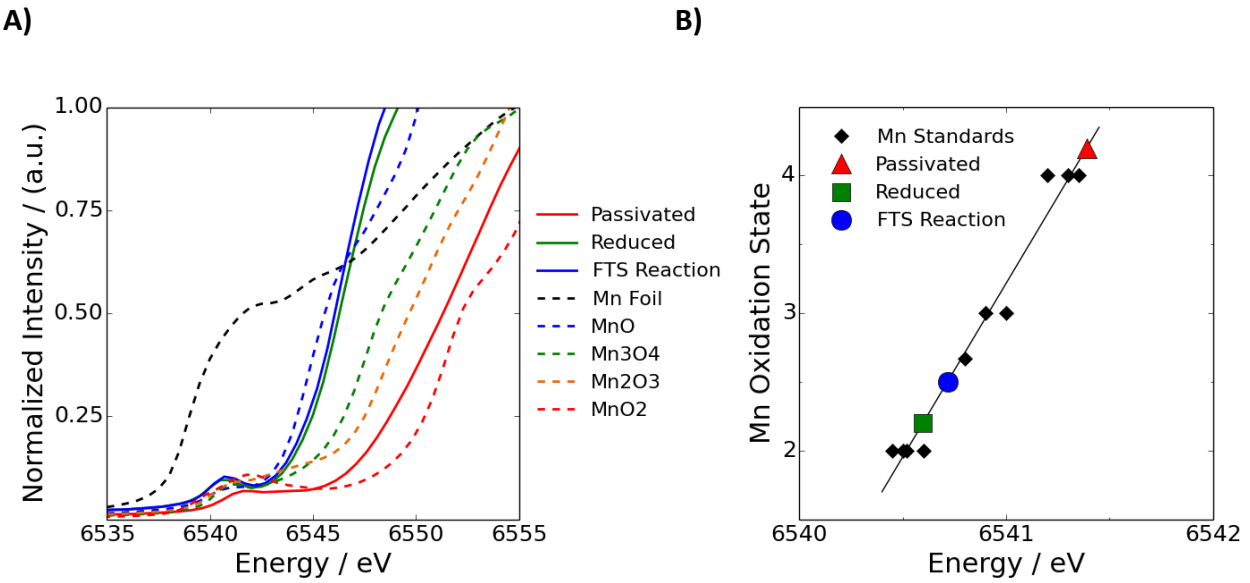

Figure 5. Mn K-edge XANES data for the Mn/Co = 0.1 catalyst. (A) XANES spectra of Mn oxide standards and the catalyst in the passivated state, after reduction, and during reaction. (B) Linear relationship between apparent Mn oxidation state and the pre-edge feature centroid. The black line is the least squares fit to the data points obtained from various Mn compounds of known oxidation state. The catalyst apparent oxidation states were inferred using this regression line. Estimates of the Mn apparent oxidation states for the catalysts with other Mn/Co ratios are reported in Table 3. The reduced catalyst data were acquired after reducing the catalysts at 673 K in H_2 for 2 h. The FTS reaction measurements were acquired after exposing the reduced catalysts to syngas at 493 K for 6 h.

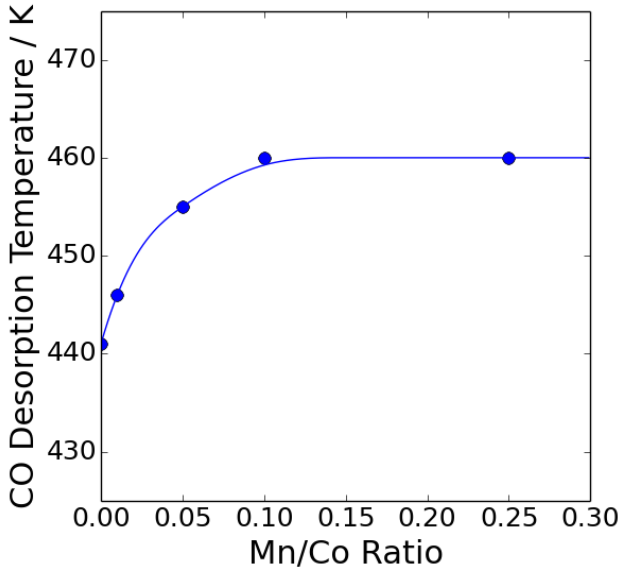

Figure 6. Mean temperature of the first chemisorbed CO desorption peak as a function of Mn loading. CO was adsorbed onto the catalyst at 213 K by pulse titration, and the temperature ramp rate for the desorption step was 10 K/min.

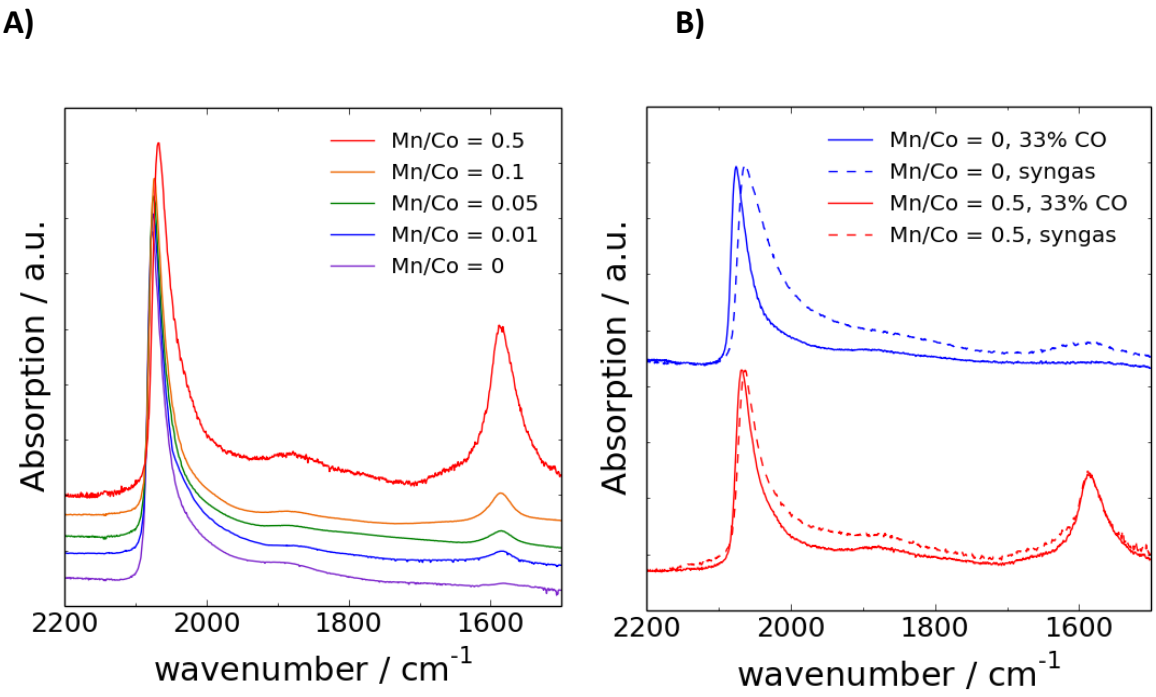

Figure 7. In situ IR spectra of adsorbed CO on the reduced Co-Mn catalysts measured at 493 K and 1 bar. (A) Comparison of Mn loadings with 100% CO. (B) Comparison of the Mn/Co = 0 and Mn/Co = 0.5 catalysts with 33% CO and either 67% He or 67% H_2 (syngas). In this figure, the signals were scaled so that the heights of the major peak near 2070 cm^{-1} are the same for each catalyst, and background subtraction was performed to remove contributions to the spectra from the catalysts and gas-phase CO.

A) B)

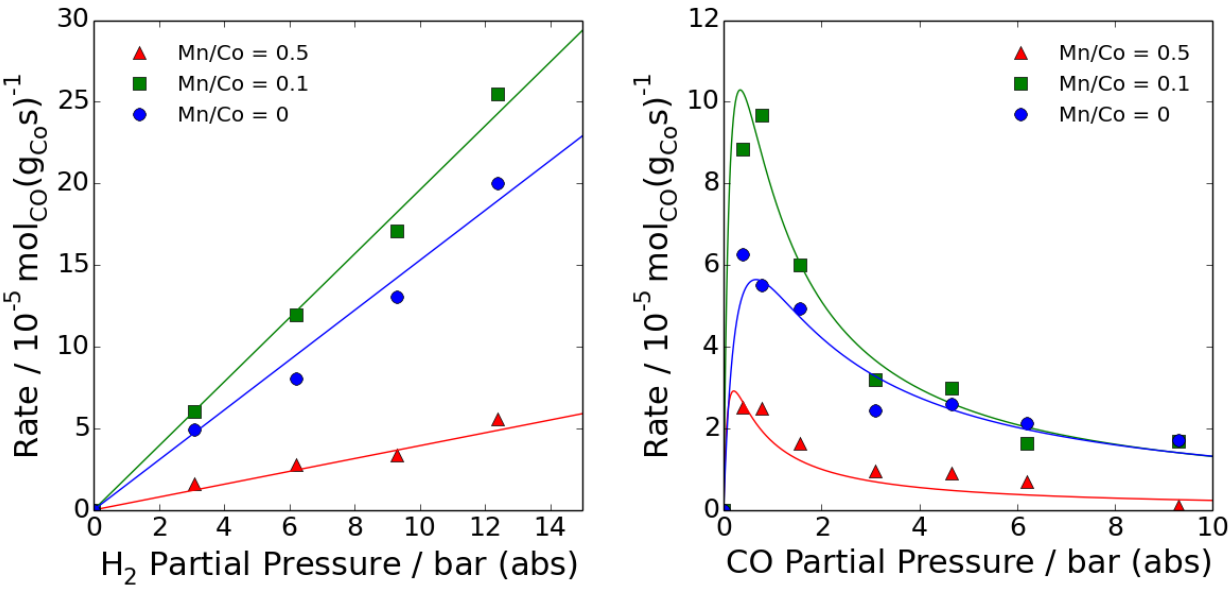

Figure 8. Dependence of CO consumption rate on (A) H_2 and (B) CO partial pressures. The variation of H_2 partial pressure was done with a constant CO partial pressure of 1.55 bar; the variation of CO partial pressure was done with a constant H_2 partial pressure of 3.1 bar. The data for both figures were collected at 493 K and were extrapolated to 0 % conversion. The curves in the plots correspond to the rate law from Eq. (3) fitted to the data.

A) B)

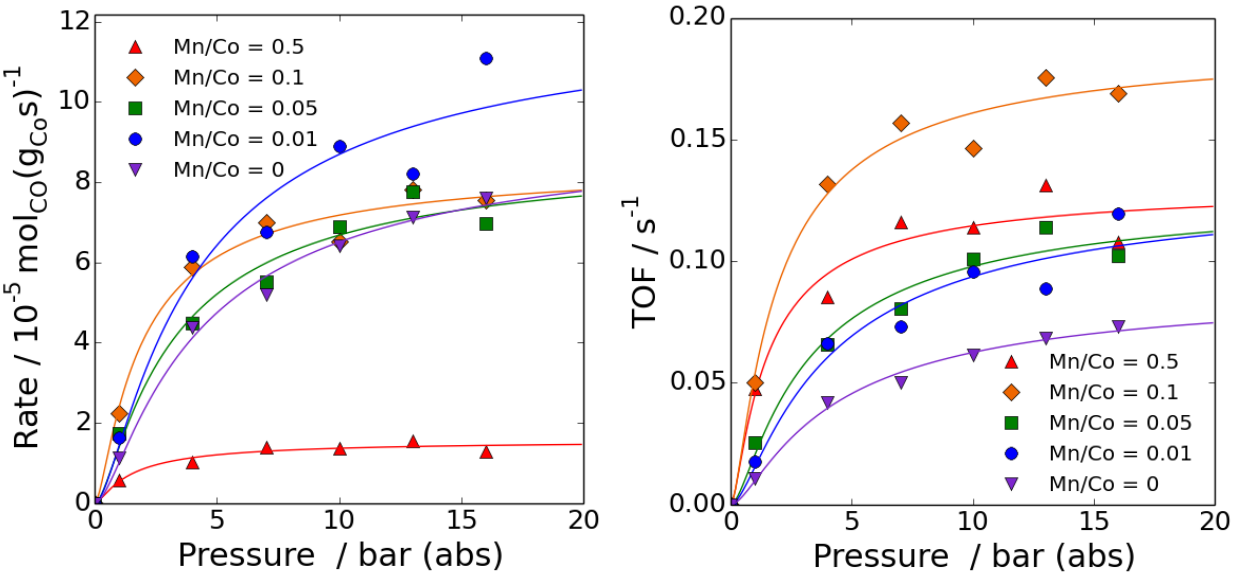

Figure 9. Comparison of (A) rates per g_{Co} and (B) turnover frequencies for different Mn/Co ratios at 493 K. The data are based on CO consumption at 0 % conversion. The curves in the plots correspond to the rate law from Eq. (3) fitted to the data.

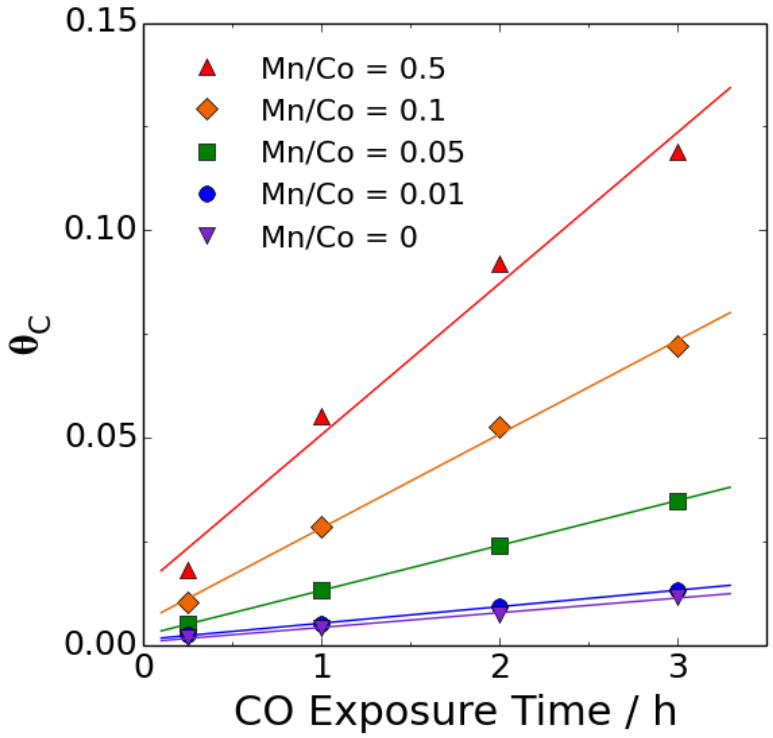

Figure 10. Fractional carbon surface coverage resulting from CO dissociation as a function of exposure time to CO at 493 K for catalysts with different Mn/Co ratios. The data are presented as the fraction of surface Co metal covered by carbon using H_2 uptake values as the basis for normalization.

A) B)

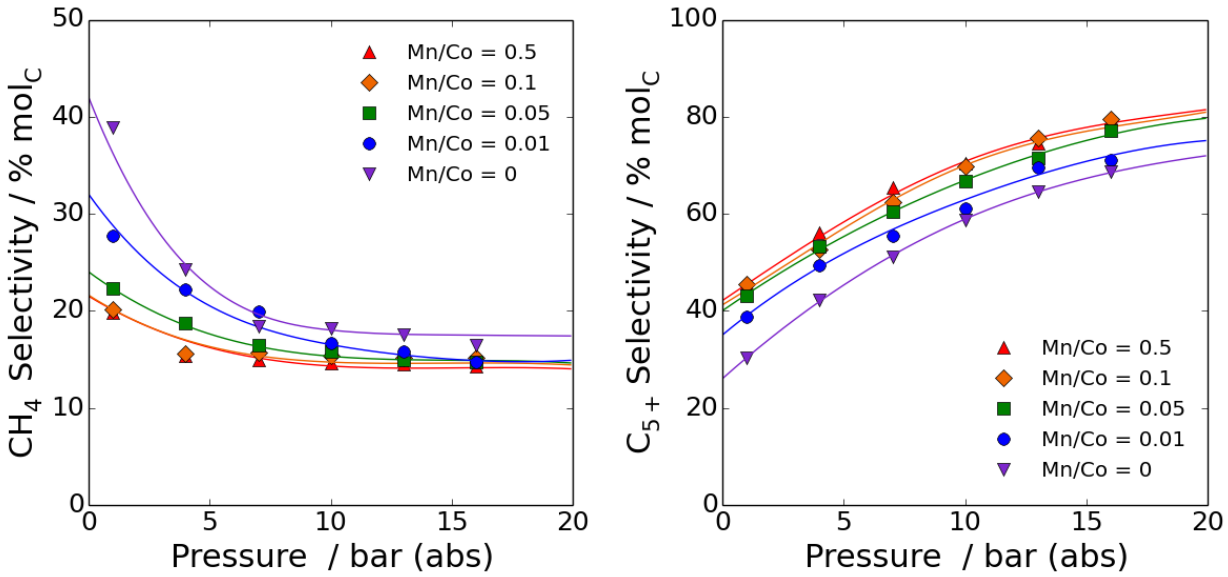

Figure 11. Comparison of (A) methane and (B) C_{5+} selectivities as a function of pressure at 493 K for catalysts with different Mn/Co ratios. The data were extrapolated to 0 % conversion. The curves in the plots are cubic splines intended for visual aid.

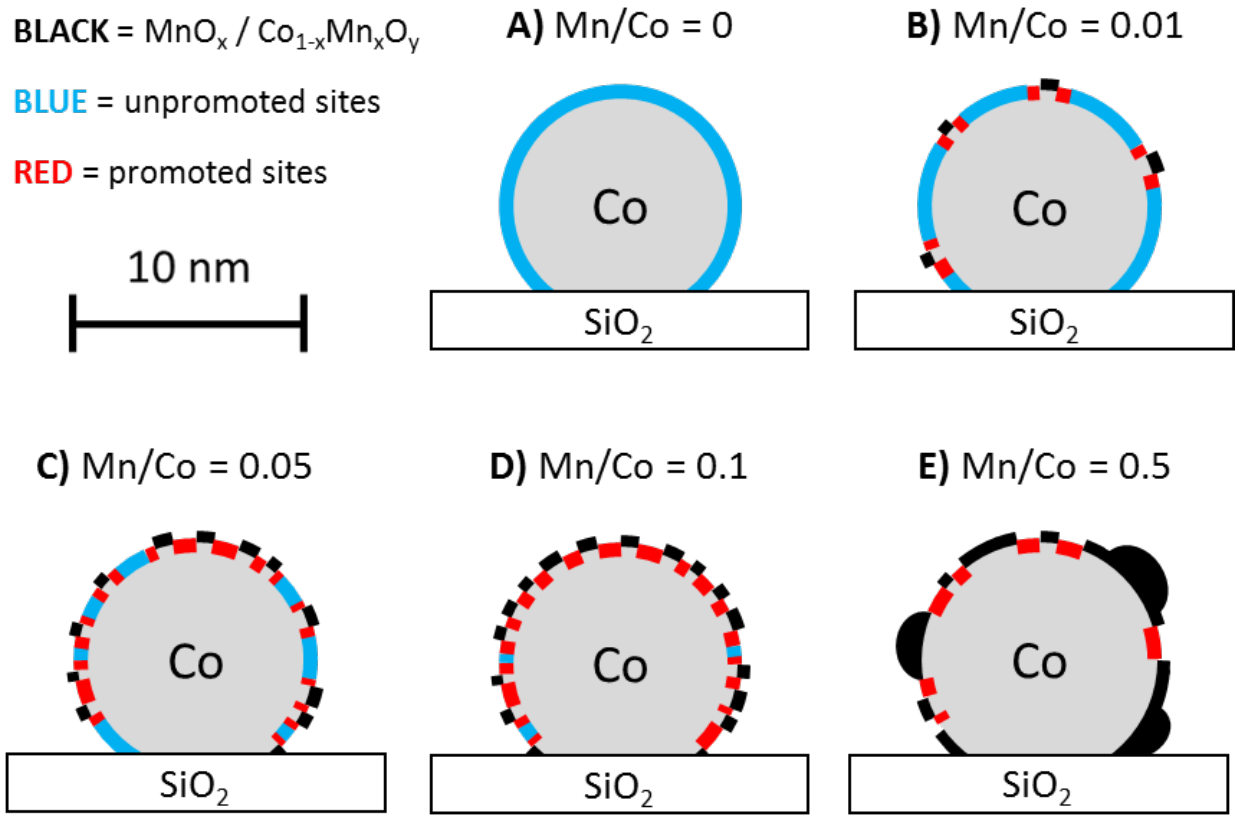

Figure 12. Hypothesized interface formation between Co and MnO_x as a function of Mn loading for (A) Mn/Co = 0, (B) Mn/Co = 0.01, (C) Mn/Co = 0.05, (D) Mn/Co = 0.1, and (E) Mn/Co = 0.5. These cartoons are drawn as 2D cross-sections through nanoparticles. The black particles decorating the surface of the Co nanoparticles are MnO_x. The outer layers of the Co nanoparticles are color-coded according to whether the Co active sites are separate from (blue) or adjacent to (red) the promoter. These cartoons are reproduced with annotations in Supporting Information, Scheme S1.

Table of Contents Figure